Weakening of Antarctic Stratospheric Planetary Wave Activities in Early Austral Spring Since the Early 2000s: A Response to Sea Surface Temperature Trends

YIHANG HU, WENSHOU TIAN, JIANKAI ZHANG, TAO WANG, MIAN XU

Key Laboratory for Semi-Arid Climate Change of the Ministry of Education, College of Atmospheric Sciences, Lanzhou University, China

*Correspondence to: wstian@lzu.edu.cn

Abstract

Using multiple reanalysis datasets and modeling simulations, the trends of Antarctic stratospheric planetary wave activities in early austral spring since the early 2000s are investigated in this study. We find that the stratospheric planetary wave activities in September have weakened significantly since 2000, which is mainly related to the weakening of the tropospheric wave sources in the extratropical southern hemisphere. As the Antarctic ozone also shows clear shift around 2000, the impact of ozone recovery on Antarctic planetary wave activity is also examined through numerical simulations. Significant ozone recovery in lower stratosphere changes the atmospheric state for wave propagation to some extent, inducing a slight decrease of vertical wave flux in upper troposphere and lower stratosphere (UTLS). However, the changes of wave propagation environment in middle and upper stratosphere over subpolar region are not significant. The ozone recovery has minor contribution to the significant weakening of stratospheric planetary wave activity in September. Further analysis indicates that the trend of September sea surface temperature (SST) over 20°N-70°S is statistically well linked to the weakening of stratospheric planetary wave activities. The model simulations reveal Numerical simulations support the result that the SST trend in the extratropical southern hemisphere (20°S-70°S) and the tropics (20°N-20°S) induce athe weakening of wave-1 component of tropospheric geopotential height in the extratropical southern hemisphere, which subsequently leads to athe decrease in stratospheric wave flux. The responses of stratospheric wave activities in the southern hemisphere to stratospheric ozone recovery is not significant in

~~simulations.~~ In addition, both reanalysis data and numerical simulations indicate that the Brewer-Dobson circulation (BDC) related to wave activities in the stratosphere has also been weakening in early austral spring since 2000 due to the trend of September SST in the tropics and extratropical southern hemisphere.

Key words: *Antarctic; Stratospheric planetary wave activities; Tropospheric wave sources; Sea surface temperature*

1. Introduction

The stratospheric planetary wave activities have important influences on stratospheric temperature (e.g., Hu & Fu, 2009; Lin et al., 2009; Li & Tian, 2017; Li et al., 2018), polar vortex (e.g., Kim et al., 2014; Zhang et al., 2016; Hu et al., 2018) and distribution of chemical substances (e.g., Gabriel et al., 2011; Ialongo et al., 2012; Kravchenko et al., 2011; Zhang et al., 2019a). Meanwhile, the stratospheric circulation modulated by planetary waves can exert impacts on tropospheric weather and climate (e.g., Haigh et al., 2005; Zhang et al., 2019b) through downward control processes (Haynes et al., 1991), which is useful for extended forecast by using preceding signals in the stratosphere (e.g., Baldwin et al., 2001; Wang et al., 2020).

The planetary perturbations generated by large-scale topography, convection and continent-ocean heating contrast can propagate from the troposphere to the stratosphere (Charney & Drazin, 1961) and form stratospheric planetary waves. As the land-sea thermal contrast in the northern hemisphere is larger than that in the southern hemisphere and produces stronger zonal forcing for the genesis of stratospheric waves, the majority of attention has been given to wave activities and their impacts on weather and climate in the northern hemisphere (e.g., Kim et al., 2014; Zhang et al., 2016; Hu et al., 2018). However, planetary wave activities in the southern hemisphere also play an important role in heating the stratosphere dynamically (e.g., Hu & Fu, 2009; Lin et al., 2009), which suppresses Polar Stratospheric Clouds (PSCs) formation and ozone depletion (e.g., Shen et al., 2020a; Tian et al., ~~2018~~2017). The Antarctic sudden stratospheric warming (SSW) that occurred in 2002 (e.g., Baldwin et al., 2003; Nishii & Nakamura, 2004; Newman & Nash, 2005) and 2019 (e.g., Yamazaki el al., 2020; Shen et al., 2020a; Shen et al., 2020b) ~~were~~ was associated with significant upward propagation of wave flux. Such episodes are extraordinarily rare in the history, and the one in 2019 contributed to the formation of the smallest Antarctic ozone hole on record (WMO, 2019). In addition, some studies reported that wildfires in Australia at the end of 2019 are related to negative phase of the Southern Annular Mode (SAM), which was induced by the extended influence of the SSW event that occurred in September (Lim et al., 2019; Shen et al., 2020b). In a word, the Antarctic planetary wave activities are important for the stratosphere-troposphere interactions and climate system in the southern hemisphere.

Long-term observations in the Antarctic stratosphere show a significant ozone decline from the early 1980s to the early 2000s due to anthropogenic emission of chlorofluorocarbons (CFCs) (WMO, 2011) and a recovery signal since 2000s because of phasing out CFCs in response to Montreal ~~Protocal~~ Protocol (e.g., Angell and Free, 2009; Krzyścin, 2012; Zhang et al., 2014; Banerjee et al., 2020). The Antarctic stratospheric ozone depletion and recovery have important impacts on climate in the southern hemisphere. The ozone depletion cools the Antarctic stratosphere through reducing absorption of radiation and leads to the strengthening of Antarctic polar vortex during austral spring (e.g., Randel & Wu, 1999; Solomon et al., 1999; Thompson et al., 2011). The anomalous circulation in the Antarctic stratosphere during austral spring exerts impacts on tropospheric circulations (e.g., intensification of SAM index, poleward shift of tropospheric jet position and expansion of the Hadley cell edge) in the subsequent months (e.g., Thompson et al., 2011; Swart & Fyfe, 2012; Son et al., 2018; Banerjee et al., 2020) and influences the distribution of precipitation and dry zone in the southern hemisphere (e.g., Thompson et al., 2011; Barnes et al., 2013; Kang et al., 2011). Following the healing of ozone loss in the Antarctic ozone hole since 2000s (e.g., Solomon et al., 2016; Susan et al., 2019), great attention has been paid on possible impacts of ozone recovery on climate system in the southern hemisphere (e.g., Son et al., 2008; Barnes et al., 2013; Xia et al., 2020; Banerjee et al., 2020). Son et al. (2008) implemented the Chemistry-Climate Model Validation (CCMVal) models to predict the response of the southern hemisphere westerly jet to stratospheric ozone recovery. Based on the Phase 5 of Coupled Model Intercomparison Projects (CMIP5) models, Barnes et al. (2013) proposed that the tropospheric jet and dry zone edge no longer shift poleward during austral summer since the early 2000s due to ozone recovery. Banerjee et al. (2020) analyzed observations and reanalysis datasets. They found that following the ozone recovery after 2000, the increase of SAM index and the poleward shifting of tropospheric jet position as well as the Hadley cell edge all experienced a pause. Their results suggest that ozone depletion and recovery have made important contributions to the climate shift that occurred around 2000 in the southern hemisphere.

However, some previous studies have reported zonally asymmetric warming patterns in Antarctic stratosphere, which are generated by increased planetary wave activities during austral spring from the early 1980s to the early 2000s (Hu & Fu, 2009; Lin et al., 2009). Note that the Antarctic stratosphere was experiencing radiative cooling in the same period due to ozone depletion (e.g., Randel & Wu, 1999; Solomon~~ et al.~~, 1999; Thompson et al., 2011). The increase in stratospheric planetary wave activities cannot be explained by ozone decline, because the acceleration of stratospheric circumpolar wind caused by radiative cooling induces more wave energy to be reflected back to the troposphere (e.g., Andrews et al., 1987; Holton et al., 2004). Hu & Fu (2009) attributed the increase in Antarctic stratospheric wave activities to the SST trend from the 1980s to the 2000s. Their results indicate that in addition to ozone change, other factors such as changes in SST ~~SST trend~~ also contribute to climate change in the southern hemisphere. Moreover, the phase of Interdecadal Pacific Oscillation (IPO) also changed at around 2000 (e.g., Trenberth et al., 2013). SST variation influences Rossby wave propagation and tropospheric wave sources, and thereby indirectly affects stratospheric wave activities (e.g., Lin et al., 2012; Hu et al., 2018; Tian et al., ~~2018~~2017). The questions here are: (1) Has the trend of stratospheric planetary wave activity~~ trend~~ in the southern hemisphere been shifting since the 2000s? (2) What are the factors responsible for the trend of Antarctic stratospheric planetary wave activity since the 2000s?

In this study, we reveal the trend of Antarctic planetary wave activity in early austral spring since the 2000s based on multiple reanalysis datasets. We also conduct sensitive experiments forced by linear increments of ozone and SST fields since the 2000s to investigate the response of Antarctic planetary activity to above two factors. The remainder of the paper is organized as follows. Section 2 describes the data, methods and configurations of model simulations. Section 3 presents the trends of stratospheric and tropospheric wave activities in early austral spring. Section 4 examines the impact of ozone recovery on Antarctic stratospheric planetary wave activity. Section ~~4~~ 5 investigates the connections between the trends of SST and stratospheric wave activities. Sections 6~~5~~ discusses the responses of tropospheric wave sources and stratospheric wave activiti~~y~~es to SST ~~trend~~ changes based on model simulations. Major conclusions and discussion are presented in Section 7~~6~~.

2. Datasets, methods and experimental configurations

a. Datasets

In this study, daily and monthly mean data extracted from the Modern-Era Retrospective analysis for Research and Applications Version 2 (MERRA-2; Bosilovich et al., 2015) dataset are used to calculate trends of ~~zonally averaged zonal wind and temperature,~~ Brewer-Dobson circulation (BDC), tropospheric wave sources, and the Elisassen-Palm (E-P) flux and its divergence in September. To verify the trend of stratospheric E-P flux, we also refer to the results derived from the European Centre for Medium-range Weather Forecasting (ECMWF) Interim Reanalysis (ERA-Interim;

Dee et al., 2011) dataset, the Japanese 55-year Reanalysis (JRA-55; Kobayashi et al., 2015) dataset and the National Centers for Environmental Prediction-Department of Energy Global Reanalysis 2 (NCEP-2; Kanamitsu et al., 2002) dataset.

The observed total column ozone (TCO) data are extracted from SBUV v8.6 satellite dataset, which is a monthly and zonal mean dataset on 5° grid. Ozone data derived from MERRA-2 dataset are also used to calculate TCO.

SST data are extracted from the Extended Reconstructed Sea Surface Temperature (ERSST) dataset, which is a global monthly mean sea surface temperature dataset derived from the International Comprehensive Ocean-Atmosphere Dataset (ICOADS). The ERSST is on global 2°×2° grid and covers the period from January 1854 to the present. We use the ~~newest~~ latest version (version 5, i.e., v5) dataset to calculate trends and correlations, and produce SST forcing field for model simulations. More details about this version of ERSST can be found in Huang et al. (2017).

In addition, the unfiltered Interdecadal Pacific Oscillation (IPO) index derived from the ERSST v5 dataset is also used in this study. ~~The IPO index is available at https://psl.noaa.gov/data/timeseries/IPOTPI/tpi.timeseries.ersstv5.data and m~~More detailed information about the index can be found in Henley et al. (2015).

b. Diagnosis of wave activities and Brewer-Dobson circulation

Planetary wave activities are measured by E-P flux ($\vec{F} \equiv (0, F^{(\phi)}, F^{(z)})$) and its divergence D_F. Their algorithms are expressed by Eqs. (1)-(3) (Andrews et al., 1987):

$$F^{(\phi)} = \rho_0 a \cos\phi(\bar{u}_z \overline{v'\theta'} / \bar{\theta}_z - \overline{v'u'}) \quad (1)$$

$$F^{(z)} = \rho_0 a \cos\phi\{[f - (a\cos\phi)^{-1}(\bar{u}\cos\phi)_\phi]\overline{v'\theta'} / \bar{\theta}_z - \overline{w'u'}\} \quad (2)$$

$$D_F = \frac{\nabla \cdot \vec{F}}{\rho_0 a \cos\phi} = \frac{(a\cos\phi)^{-1}\frac{\partial}{\partial\phi}(F^{(\phi)}\cos\phi) + \frac{\partial F^{(z)}}{\partial z}}{\rho_0 a \cos\phi} \quad (3)$$

where u, v represent zonal and meridional components of horizontal wind, w is vertical velocity, θ is potential temperature, a is the Earth radius, f is the Coriolis parameter, z is geopotential height, ϕ is latitude, ρ_0 is the background air density.

The quasi-geostrophic refractive index (RI) is used to diagnose the environment of wave propagation (Chen & Robinson, 1992). Its algorithm is written as Eq. Equation (4):

$$RI = \frac{\bar{q}_\varphi}{\bar{u}} - \left(\frac{k}{a\cos\varphi}\right)^2 - \left(\frac{f}{2NH}\right)^2 \quad (4)$$

where the zonal-mean potential vorticity meridional gradient $\bar{q}_\varphi$ is

$$\bar{q}_\varphi = \frac{2\Omega}{a}\cos\varphi - \frac{1}{a^2}\left[\frac{(\bar{u}\cos\varphi)_\varphi}{a\cos\varphi}\right]_\varphi - \frac{f^2}{\rho_0}\left(\rho_0 \frac{\bar{u}_z}{N^2}\right)_z \quad (5)$$

H, q, k, N^2 and Ω are the scale height, potential vorticity, zonal wave number, buoyancy frequency, and Earth's angular frequency, respectively.

域代码已更改

The Brewer-Dobson circulation driven by wave breaking in the stratopause stratosphere is closely related to stratospheric wave activities. Its meridional and vertical components $(\bar{v}^*, \bar{w}^*)$ and stream function ($\psi^*(p,\phi)$) are expressed by Eqs. (4)-(6) (Andrews et al., 1987; Birner & Bönisch, 2011) :

$$\bar{v}^* \equiv \bar{v} - \rho_0^{-1}(\rho_0 \overline{v'\theta'} / \bar{\theta}_z)_z \quad (6)$$

$$\bar{w}^* \equiv \bar{w} + (a\cos\phi)^{-1}(\cos\phi \cdot \overline{v'\theta'} / \bar{\theta}_z)_\phi \quad (7)$$

$$\psi^*(p,\phi)=\int_0^p \frac{-2\pi a\cdot\cos\phi\cdot\bar{v}^*(p'',\phi)}{g}dp'' \qquad (8)$$

where p is the air pressure, π is the circular constant, g is the gravitational acceleration.

In Eqs. (1)-(8), the overbar and prime denote a zonal mean and departure from the zonal mean, respectively. The subscripts denote partial derivatives. The Fourier decomposition is used to obtain components of Eqs. (1)-(3) with different zonal wave numbers. Meanwhile, the Fourier decomposed components of geopotential height zonal deviations are also used to determine tropospheric wave sources.

c. Statistical methods

The trend is measured by the slope of linear regression based on the least square estimation. The correlation is used to analyze statistical links between different variables. In this paper, all the time series have been linearly detrended before calculating correlation coefficients (r) and their corresponding significances.

The change-point testing (e.g. Banerjee et al., 2020) is used to make sure the significance of trend or correlation coefficient is not unduly influenced by some particular beginning or ending years, and thereby confirm that the trend exists objectively.

We use two-tailed student's t test to calculate the significances of trend, correlation coefficient or mean difference. The result of significance test is measured by p value or confidence intervals in this paper. $p \le 0.1$, $p \le 0.05$ and $p \le 0.01$ suggest the trend, correlation coefficient or mean difference is significant at/above the 90%, 95% and 99% confidence levels, respectively. The confidence interval of trend is shown in (7) (Shirley et al., 2004):

$$[\hat{b}-t_{1-\alpha/2}(n-2)\hat{\sigma}_b, \hat{b}+t_{1-\alpha/2}(n-2)\hat{\sigma}_b] \quad (7)$$

where $\hat{b}$ is estimated value of slope, $\hat{\sigma}_b$ is standard error of slope and it is written as: $\hat{\sigma}_b = \hat{b}\cdot\sqrt{\frac{\frac{1}{r^2}-1}{n-2}}$, $t_{1-\alpha/2}(n-2)$ denotes the value of t-distribution with the degree of freedom equal to $n-2$ and the two-tailed confidence level equal to $1-\alpha$ ($\alpha = 0.90$, 0.95 or 0.99). The confidence interval of mean difference is expressed by Eq. (8) (Shirley et al., 2004):

$$[\bar{X}-\bar{Y}-t_{1-\alpha/2}(M+N-2)\cdot S_w\cdot\sqrt{\frac{1}{M}+\frac{1}{N}}, \bar{X}-\bar{Y}+t_{1-\alpha/2}(M+N-2)\cdot S_w\cdot\sqrt{\frac{1}{M}+\frac{1}{N}}] \quad (8)$$

where

$$S_w = \sqrt{\frac{1}{M+N-2}[\sum_{i=1}^{M}(X_i-\bar{X})^2+\sum_{j=1}^{N}(Y_j-\bar{Y})^2]} \quad (9)$$

Here, $\bar{X}$ and $\bar{Y}$ are the sample averages, M and N are the numbers of sample sizes with two populations, $t_{1-\alpha/2}(M+N-2)$ denotes the value of t-distribution with the degree of freedom equal to $M+N-2$ and the two-tailed confidence level equal to $1-\alpha$.

Previous studies have indicated that SST impact on the stratosphere shows a spatial dependence (e.g., Xie et al., 2020). To find out a robust relationship between the trend of SST in a specific region and the trend of stratospheric wave activities, we divide the global ocean into three regions: SH (the extratropical southern hemisphere, 70°S-20°S), TROP (the tropics, 20°S-20°N) and NH (the extratropical northern hemisphere, 20°N-70°N). Since the impacts in different regions might be combined, we also consider three combined regions named as SHtrop (the extratropical southern hemisphere and the tropics, 70°S-20°N), NHtrop (the extratropical northern hemisphere and the tropics, 20°S-70°N) and the Globe (70°S-70°N). To find statistical connections between the trend of SST and that of stratospheric wave activities, we examine the first three leading patterns (EOF1, EOF2, EOF3) and principal components (PC1, PC2, PC3) of SST in above six regions obtained from Empirical Orthogonal Function (EOF) analysis. In all the six regions, there is always one EOF mode~~s~~ that shows great similarity to the spatial pattern of trend (not shown) as we do not detrend SST time series when the EOF analysis is carried out. Thus, the significance of the correlation between the PC time series of that EOF mode and time series of stratospheric E-P flux can be used as the criterion to determine the statistical connection between the trend of SST and the trend of stratospheric wave activities.

d. The model and experiment configurations

The F_2000_WACCM_SC (FWSC) component in the Community Earth System Model (CESM; version 1.2.0) is used to verify the impacts of SST and ozone recovery trends on tropospheric wave sources and stratospheric wave activities in early austral spring. The FWSC component is the Whole Atmosphere Community Climate Model version 4 (WACCM4) with specified chemistry forcing fields (such as ozone, greenhouse gases (GHG), aerosols and so on), which have fixed values in 2000 by default. The WACCM4 includes active atmosphere, data ocean (run as a prescribed component, simply reading SST forcing data instead of running ocean model), land and sea ice. ~~Important p~~Physics schemes in the WACCM4 are based on those in the

Community Atmospheric Model version 4 (CAM4; Neale et al., 2013). The WACCM4 uses a finite-volume dynamic framework and extends from the ground to approximately 145 km (5.1×10^{-6} hPa) altitude in the vertical with 66 vertical levels. The simulations presented in this paper are conducted at a horizontal resolution of 1.9°×2.5°. More information about the WACCM can be found in Marsh et al. (2013).

Control experiments and sensitive experiments are conducted to investigate responses of Antarctic stratospheric wave activities to SST trends and the ozone recovery trend in early austral spring. For the experiments of SST trends, monthly mean global SST during 1980-2000 derived from the ERSST v5 dataset is used as SST forcing field in the control experiment (sstctrl). For the four sensitive experiments (sstNH, sstSH, ssttrop, sstSHtrop), linear increments of SST in different regions in September during 2000-2017 are used as the forcing field. Ozone, aerosols and greenhouse gases (GHG) in the control experiment and the four sensitive experiments all have the fixed values in 2000. For the experiments of ozone recovery trend, monthly mean three-dimensional global ozone during 1980-2000 derived from the MERRA-2 dataset is used as the ozone forcing field in the control experiment (O3ctrl). The sensitive experiment (O3sen) is forced by linear increments of ozone in September during 2001-2017. The SSTs in O3ctrl and O3sen both are monthly mean global SST during 1980-2000. The aerosol and greenhouse gases values in 2000 are used. These experiment configurations are summarized and listed in Table 1 and Table 2.

Firstly, we run the FWSC component to generate randomly different initial conditions for 120 years with free run. Then, each experiment includes 100 ensemble members that run from July to September forced by these initial conditions from the 21st year to the 120th year in July. The forcing fields of SST and ozone are only superposed from July to September. July and August are taken as spin-up time and simulations during this period are discarded. The ensemble mean in September derived from these 100 ensemble members is regarded as the final result of each experiment. A similar approach is implemented for sensitive experiments, in which the forcing fields superposed only in certain months. The same approach has been used in previous studies (e.g., Zhang et al., 2018).

3. Trend of planetary wave activities in early austral spring

Figure 1 shows the trends of stratospheric planetary wave activities in the southern hemisphere September during 1980-2000 and 2000-2017, respectively. Note that the vertical E-P flux entering into the stratosphere over 50°S-70°S in September has been increasing during 1980-2000, accompanied by intensified wave flux convergence in the upper stratosphere (Fig. 1a) that is mainly contributed by the wave-1 component (Fig. 1b). This feature implies that the stratospheric planetary wave activities have strengthened in early austral spring during 1980-2000. A similar result has been reported in previous studies (Hu & Fu, 2009; Lin et al., 2009). During 2000-2017, however, vertical propagation ~~transport~~ of stratospheric E-P flux weakened over the subpolar region of the southern hemisphere, which was accompanied by intensified wave flux divergence in the upper stratosphere (Fig. 1d) mainly contributed by the wave-1 component (Fig. 1e) while the wave-2 component also made certain contributions (Fig. 1f). Similar features also appear in August, but not as significant as that in September (Fig. S1). For this reason, hereafter we focus on the features in September.

The SSW that occurred in 2002 was accompanied with large upward wave fluxes in the stratosphere, which is extremely rare in history and has been studied extensively in ~~numerous~~ previous studies (e.g., Baldwin et al., 2003; Nishii & Nakamura, 2004; Newman & Nash, 2005). Since the period with a negative trend of stratospheric vertical wave flux is short, it is necessary to further investigate whether such a negative trend is artificially influenced by the single year of 2002. Therefore, following Banerjee et al. (2020), we use a change-point method to test the significance of the trend during various periods based on four reanalysis datasets (ERA-Interim, MERRA-2, JRA-55, NCEP-2). Figures 2a (including the year 2002) and 2b (excluding the year 2002) display the time series ~~(Fz)~~ of area-weighted vertical stratospheric wave flux (Fz) over the southern hemisphere subpolar region obtained from different reanalysis datasets. Note that the wave flux time series obtained from the four reanalysis datasets all present a positive trend from the early 1980s to the early 2000s and a negative trend from the early 2000s to present, regardless of whether the extreme value in 2002 is removed or not. The correlation coefficients of the time series between these reanalysis datasets are above 0.9 and statistically significant (Table 3), suggesting that the time series derived from different datasets are consistent with each other. Figures 2c-f show the trends and corresponding confidence intervals calculated with four different beginning years (1980, 1981, 1982, 1983), four different ending years (2015, 2016, 2017, 2018), and change-point years from 1998 to 2013. The trends and confidence intervals in Figures 2g-j are the same as that in Figures 2c-f, except that the extreme value in 2002 is removed. The positive trend from the early 1980s to the 21st century remains significant regardless of different beginning years and ending change-point years (Figs. 2c-j). However, Figures 2c-f and Figures 2g-j indicate that the positive value of the trend is decreasing gradually when the period is prolonged, which is apparently attributed to the negative trend with the beginning change-point year of around 2000. Although the negative trend from the change-point year to ending year becomes less significant when the value in 2002 is removed, it remains significant in some periods, which are also illustrated on diagrams of latitude-pressure profiles (Fig. S2). Therefore, the weakening of stratospheric wave activities in early austral spring since the early 2000s is robust. In this paper, we take the year 2000 as the beginning year of the weakening trend to simplify descriptions in the following discussion.

Figure 3 shows the trends of tropospheric wave sources in September since 2000. There is a significant positive trend of the wave-1 component in 500 hPa geopotential height over the southern Indian ocean and a significant negative trend over the southern Pacific, which form an out-of-phase superposition on its climatology (Fig. 3b). The trend pattern of wave-2 component is also out-of-phase with its climatology, although it is not significant (Fig. 3c). The above features still maintain when the values in 2002 are removed (Figs. S3b, c), implying that the southern hemispheric tropospheric wave sources in early austral spring have weakened since 2000, which is also reflected in the decrease of tropospheric vertical wave flux (Figs. 3d, e; Figs. S3d, e).

4. Response of Antarctic stratospheric wave activity to ozone recovery

带格式的: 列出段落, 首行缩进: 0 字符, 行距: 单倍行距, 多级符号 + 级别: 1 + 编号样式: 1, 2, 3, … + 起始编号: 1 + 对齐方式: 左侧 + 对齐位置: 0 厘米 + 缩进位置: 0.63 厘米

带格式的: 字体: 四号, 加粗, 字体颜色: 自动设置

带格式的: 字体: (默认) Times New Roman, 小四, 字体颜色: 文字 1

Previous studies have suggested that ozone depletion and recovery are important to climate shift that occurred around 2000 in the southern hemisphere during austral summer (e.g., Son et al., 2008; Thompson et al., 2011; Barnes et al., 2013; Banerjee et al., 2020). The impacts of stratospheric ozone changes on Antarctic wave propagation during austral summer has also been examined in previous studies (e.g., Hu et al., 2015). However, whether ozone recovery in September explains the weakening of stratospheric planetary waves at the same month remains unclear. The correlation between detrended time series of September Antarctic total column ozone (TCO) derived from SBUV and stratospheric vertical wave flux (Fz) is 0.70 ($p=0.0011$) during 2000-2017. The increase of wave activity in polar stratosphere causes heating effects and suppresses the formation of PSCs, and hence, slow down the ozone depletion (e.g., Shen et al. 2020a). Therefore, the Antarctic ozone and stratospheric wave activity show statistically significant positive correlation. Theoretically, heating effects caused by ozone recovery in Antarctic stratosphere may also decelerate the Antarctic stratospheric polar vortex and induce more waves to propagate into stratosphere (Andrews et al., 1987; Holton et al., 2004). These preliminary analysis cannot verify that the ozone recovery is responsible for weakening of stratospheric wave activity. The role of ozone recovery in stratospheric wave changes needs to be further explored by model simulations. In this section, we use a group of time-slice experiments (O3ctrl and O3sen) to address this issue.

Figure 4 shows the time series and piecewise trends of September TCO in the Antarctic during 1980-2017. As reported by previous studies (e.g., Angell and Free,

带格式的: 缩进: 首行缩进: 2 字符

2009; Banerjee et al., 2020; Krzyścin, 2012; Solomon et al., 2016; WMO, 2011; Zhang et al., 2014), the Antarctic ozone show a significant decline during 1980-2000 (Figs. 4a, b, c) and a slight recovery during 2001-2017 (Figs. 4a, d, e). The recovery trend is calculated with data in 2002 removed because the large poleward transport induced by SSW in 2002 leads to extreme values of ozone (e.g. Solomon et al., 2016). In addition, the correlation of TCO between MERRA-2 and SBUV datasets is 0.61 ($p=4.5\times10^{-5}$), suggesting the changes of TCO derived from the reanalysis dataset and the observations have a good consistency. Thus, in order to get three-dimensional structure of ozone changes, the ozone data from MERRA-2 are used to make forcing fields for CESM. As described in Section 2, a control experiment (O3ctrl) forced by climatological ozone and a sensitive experiment forced by the linear increment of global ozone in September during 2001-2017 are conducted to explore the impacts of ozone recovery. The pattern of ozone forcing fields is similar to its trend patterns (Figs. 4d, e; Figs. 5a, b). Other details of these two experiments have been given in Section 2 and Table 2.

Fig. 6 and Fig. 7 show the responses of wave activity and wave propagation environment forced by O3sen. Note that the significant ozone recovery over south pole mainly appears in lower stratosphere (about 200 hPa to 50 hPa) (Fig. 4e). In most southern polar regions from 50 hPa to 3 hPa, the ozone recovery is not significant (Fig. 4e). The features are attributed to limitation of ODSs emission and reduction of heterogeneous reaction on PSCs, which mainly distribute in lower stratosphere (e.g., Solomon, 1999). Ozone recovery in polar lower stratosphere absorbs more ultraviolet radiation and causes cooling in Antarctic troposphere (Fig. 6b). To maintain thermal balance, zonal wind accelerates below 200 hPa over 60°S-70°S (Fig. 6a).

The changes of zonal wind and temperature forced by ozone recovery induce changes in wave propagation environment. The refractive index (RI) is a good matric to reflect the atmosphere state for wave propagation. Theoretically, planetary waves tend to propagate into large RI regions (Andrews et al., 1987). The responses of RI and its terms are shown in Figs. 6c-f. Note that the second term of RI does not change with atmospheric state and the third term of RI is insignificant compared to the first term (Hu et al., 2019). Previous studies indicate that changes in zonal mean potential vorticity meridional gradient $\bar{q}_\varphi$ could explain the changes in RI in middle and high latitudes (e.g. Hu et al., 2019; Simpson et al., 2009). Consistent with these studies, the pattern of $\bar{q}_\varphi$ show some similarity with pattern of RI (Figs. 6c, d), especially in lower stratosphere over subpolar regions (Figs. 6c, d). According to the Eq. (5), the first term of $\bar{q}_\varphi$ does not change with atmospheric state. Therefore, the second term ($-[\frac{(\bar{u}\cos\varphi)_\varphi}{\cos\varphi}]_\varphi$, hereafter uyy term or barotropic term) and the third term ($-\frac{f^2}{\rho_0}(\rho_0\frac{\bar{u}_z}{N^2})_z$, hereafter uzz term or baroclinic term) are investigated. Note that the pattern of responses in baroclinic term is similar with $\bar{q}_\varphi$ (Figs. 6d, f). The uzz term also can be written as $(\frac{f^2}{HN^2}+\frac{f^2}{N^4}\frac{dN^2}{dz})\bar{u}_z-\frac{f^2}{N^2}\bar{u}_{zz}$. Meanwhile, zonal wind acceleration in upper troposphere weakens the vertical shear of u ($\bar{u}_z$) around 200 hPa over subpolar regions, inducing a decrease of baroclinic term and RI in upper troposphere and lower stratosphere (UTLS) over 60°S-70°S (Figs. 6d, f). The response of RI induce a slight decrease of vertical wave flux in UTLS over subpolar regions (Fig.

域代码已更改
域代码已更改
域代码已更改
域代码已更改
带格式的: 字体: 小四
带格式的: 字体: 小四
域代码已更改
域代码已更改
域代码已更改
域代码已更改

7a), which is mainly contributed by its wave-1 component (Fig. 7b). However, the changes of wave activity in UTLS are not significant in ensemble mean of simulations (Figs. 7a, b, c). Meanwhile, note that the responses of zonal wind and temperature to ozone recovery are not significant above 50 hPa over subpolar regions (Figs. 6a, b), inducing negligible changes of wave propagation environment (Fig. 6c) and wave activity (Fig. 7) in middle and upper stratosphere.

In a word, the significant ozone recovery in Antarctic lower stratosphere changes wave propagation in upper troposphere and lower stratosphere to some extent. However, these weak responses still cannot explain the significant decrease of stratospheric wave flux in September.

4.5. Role of SST trends in the weakening of Antarctic stratospheric wave activities

In this section, we further explore factors ~~that lead to~~responsible for the weakening of tropospheric wave sources and stratospheric wave activities since the early 2000s in early austral spring. Many~~Numerous~~ studies reported that ~~the~~ SST variations ~~in sea surface temperature~~ can affect stratospheric climate (e.g., Li, 2009; Hurwitz et al., 2011; Lin et al., 2012; Hu et al., 2014; Hu et al., 2018; Tian et al., ~~2018~~2017; Xie et al., 2020). Hu & Fu (2009) also attributed the strengthened stratospheric wave activities in the southern hemisphere to SST trend from the early 1980s to the early 2000s. Furthermore, global SST in September during 2000-2017 also has a significant trend. The significant warming pattern is mainly found over the southern Indian ocean, the southern Atlantic ocean, the eastern and western equatorial Pacific, the western equatorial and Northern

Atlantic ocean (Fig. ~~4b~~8b). A significant cooling pattern is located over the southeast Pacific (Fig. ~~4b~~8b). In addition, the transitions around 2000 exist in SST time series over some regions. In the southern Indian ocean, SST shows insignificant trend during 1980-2000 and significant warming trend during 2000-2017 (Fig. 8c). The subtropical Pacific ocean in east of Australia is linked with the Pacific-Southern America (PSA) wave train (e.g. Shen et al., 2020b), and the SST there shows significant warming trend during 1980-2000 and insignificant trend during 2000-2017. The SST in southeast Pacific shows insignificant trend during 1980-2000 and significant cooling during 2000-2017 (Fig. 8e). Trends of SST in southern Atlantic ocean are opposite during these two piecewise periods, showing significant cooling during 1980-2000 and significant warming during 2000-2017. It is apparent that the ~~In a word, the~~ spatial pattern of SST trend during 2000-2017 is obviously different from that during 1980-2000 (Fig. ~~4a~~8a, b), which may affect the tropospheric wave sources. Thus, it is necessary to analyze the connection between SST trend and wave activity trend since the early 2000s.

Figure ~~5~~ 9 shows the significance of the trend of principle component (PC) time series ~~trends (Figs. 5a-f)~~ of SST in different regions (Figs. 9a-f), and the significance of correlations (Figs. ~~5g~~9g-l) between the PC time series and Fz in September during various periods~~ in September~~. The trend of PC1 time series in SH region is significant during serval periods (Fig. ~~5a~~9a), while the correlation between PC1 and Fz is only significant with the particular ending year of 2015 (Fig. ~~5g~~9g). This feature suggests that the connection between the SST trend in SH region and the trend of stratospheric wave activity is not robust. The correlation between trend of stratospheric wave activity and that of SST in TROP or NH region is also weak (Fig. ~~5e~~9e, f). As for the combined regions, note that the PC2 time series in SHtrop region has a significant trend (Fig. ~~5d~~9d) and the correlation between the PC2 time series in SHtrop and Fz with the beginning year of around 2000 is also significant (Fig. ~~5j~~9j) regardless of different ending years. This feature implies that the extratropical southern hemisphere and tropical SST has a robust connection with stratospheric wave activities in early austral spring since the early 2000s. The correlations between Fz and all PC time series in NHtrop (Fig. ~~5k~~9k) and Globe (Fig. ~~5l~~9l) region are not as robust as that between Fz and PC2 time series in SHtrop region (Fig. ~~5j~~9j), indicating that the connection between SST trend in extratropical northern hemisphere and the trend of stratospheric wave activity is weak.

Figure ~~6~~ 10 shows the first three EOF modes of September SST in SHtrop region during 2000-2017. The second mode (Fig. ~~6b~~10b) shows a great similarity to the spatial pattern of SST trend (Fig. ~~4b~~8b), and the corresponding PC2 time series also has a significant trend (slope=1.71, p<0.01). The correlation between PC2 and ~~the~~ Fz is significant (r=-0.56, p=0.016) and the correlation coefficient remains significant (r=-0.46, p=0.065) at the 90% confidence level when the value in 2002 is removed. This result suggests that the SST trend in SHtrop region is closely related to the recent weakening of stratospheric wave activities. The first EOF mode is similar to IPO (Fig. ~~6a~~10a) and its corresponding principal component is ~~highly~~ significantly correlated (r=-0.98, p<0.01) with the unfiltered IPO index. However, it shows no significant trend (Fig. ~~6d~~10d) and has no significant correlation (Fig. ~~6g~~10g) with stratospheric wave flux, implying that the linkage between the IPO phase change at around 2000 (e.g. Trenberth et al., 2013) and the weakening of Antarctic stratospheric wave activities is weak. The correlation between PC3 and Fz is also not significant (Fig. ~~6i~~10i). Therefore, it is possible that the combined effect of SST trend (the second EOF mode) in the tropical and extratropical southern hemisphere leads to the weakening of stratospheric wave activities in early austral spring since the early 2000s.

~~5.~~6. Simulated changes in Antarctic stratospheric wave activities forced by SST trends

The analysis in Section ~~4~~ 5 suggests that the SST changes~~trend~~ in SHtrop region may contribute to the weakening of the southern hemispheric stratospheric wave activities. Here, numerical experiments sstNH, sstSH, ssttrop and sstSHtrop forced by linear increments of SST in September during 2000-2017 (Fig. ~~7~~11; more details can be found in Section 2) are conducted to verify the results presented ~~discussed~~ in Section ~~4~~5.

Figure ~~8~~ 12 shows the simulated response of 500 hPa geopotential height to SST changes in different regions. The climatological distributions of the wave-1 component (Figs. ~~8b~~12b, e, h, k) and the wave-2 component (Figs. ~~8c~~12c, f, i, l) from the simulations are consistent with that from reanalysis dataset (Figs. ~~4b~~3b, c), indicating that the model can well capture spatial distributions of the atmospheric waves. Note that the ~~Fourier component (~~wave-1 and wave-2~~)~~ anomalies simulated with SST changes in SH, TROP and SHtrop are all ~~are~~ significant. They superpose on the corresponding climatological patterns in an out-of-phase style (Figs. ~~8e~~12e, f, h, i, k, l), indicating that the changes in SST ~~SST trends~~ in SH, TROP and SHtrop lead to a weakening of tropospheric wave sources in the extratropical southern hemisphere. However, ~~the 500 hPa geopotential height anomaly of~~ the predominate wave-1 component of the 500 hPa geopotential height anomaly in the extratropical southern hemisphere forced by the experiment with NH SST change is relatively weak (Fig. ~~8b~~12b). This feature suggests that the SST changes ~~trend~~ in extratropical northern hemisphere are~~is~~ incapable of inducing a robust response of tropospheric wave sources in the extratropical southern hemisphere.

Figure ~~9~~ 13 shows the simulated responses of stratospheric wave activities in the southern hemisphere to SST changes ~~in~~ over different regions. It is apparent~~found~~ that the experiments with SST changes in SH, TROP and SHtrop show significantly weakened stratospheric wave activities (Figs. ~~9~~13d, g, j), which are mainly attributed to the responses of the wave-1 component (Figs. ~~9~~13e, h, k). These results are consistent with the responses of tropospheric wave sources (Figs. ~~8~~12d, e, g, h, j, k). However, there are no significant anomalies of stratospheric wave flux in the subpolar region ~~as exhibited~~ in Figures ~~9~~13a and ~~9~~13b, which is consistent with the response of corresponding tropospheric wave sources (Figs. ~~8~~12a, b) and the weak correlation between Fz and PC time series of SST in NH region (Fig. ~~5~~9i). The result here ~~It~~ suggests that the response of southern hemisphere stratospheric wave activities to SST trend in NH region is weak.

The r~~R~~esults of all these experiments are summarized and displayed in Figure ~~10~~14, which ~~is~~ are quantified by the frequency distribution of southern hemisphere stratospheric vertical wave flux derived from the 100 ensemble members of each experiment. Compared to the blue fitting curves, the red fitting curves shift to the left as shown in Figs. ~~10b~~14b, ~~10c~~ 14c and ~~10d~~14d, suggesting that the SST changes in SH, TROP and SHtrop regions weaken the upward propagation of stratospheric wave flux. The area-weighted anomalies of vertical E-P flux in the subpolar region of the southern hemisphere induced by SST changes in SH, TROP and SHtrop regions are -0.084×10^5 $kg\cdot s^{-2}$, -0.12×10^5 $kg\cdot s^{-2}$ and -0.13×10^5 $kg\cdot s^{-2}$, respectively. The sum of the anomalies forced by sstSH and ssttrop is not equal to the anomaly forced by sstSHtrop, which may be resulted from non-linear interactions between the responses of wave activities to SST trends in SH region and TROP region. The weakening of stratospheric wave activities forced by SST increment in the tropical region is ~~more obvious and~~ more significant than that in extratropical southern hemisphere (Figs. ~~10b~~14b, c, e), implying that the SST trend in the tropical region contributes more to the weakening of stratospheric wave activities since 2000. Meanwhile, it is apparent that the weakening of the southern hemisphere stratospheric wave activities forced by sstSHtrop is the most significant among all the sensitive experiments (Fig. ~~10e~~14e). The reduction of vertical E-P flux over (50°S-70°S, 200 hPa-10 hPa) forced by sstSHtrop is approximately 12%. These modeling ~~simulation~~ results indicate that the weakening of the Antarctic stratospheric wave activities in September since 2000 is induced mainly by the combined effects of SST trends in the tropical and extratropical southern hemisphere. It also explains why the independent correlation between Fz and PC time series obtained over~~for~~ SH or TROP region is not as significant as that between Fz and PC time series obtained over ~~for~~ SHtrop region (Figs. ~~5g~~9g, h, j). Moreover, the mean linear increment of area-weighted vertical E-P flux from 200 hPa to 10 hPa over 70°S-50°S in September during 2000-2017 derived from four reanalysis datasets is about -0.38×10^5 kg·s^{-2}. Therefore, the contribution of SST trend over 20°N-70°S (the SHtrop region) to the weakening of stratospheric activities is approximately 34%.

In addition, the reanalysis datasets show that the Brewer-Dobson circulation related to wave activities in the stratosphere weakened significantly in early austral spring during 2000-2017 (Fig. 15b), which is contrary to the intensified trend during 1980-2000 (Fig. 15a). The transition of BDC around 2000 is believed to be associated with ozone depletion and recovery (e.g., Polvani et al., 2017; Polvani et al., 2018). However, our modeling results suggest that the SST trend is responsible for the weakening of BDC in September since 2000 (Figs. 15d, e, f), The response of BDC to ozone recovery is not significant (Fig. 15c) in September, especially for the branch near the Antarctic. These results indicate that apart from the ozone depletion and recovery the SST trend should also be taken into consideration when exploring the mechanism for the climate transition in the southern hemispheric stratosphere around 2000.

Previous studies reported that there is usually a time lag for tropic SST to affect extratropical circulation (e.g., Shaman & Tziperman, 2011). Thus, the impact of tropical SST change before September needs to be further examined. Our simulations indicate that the tropical SST trend in September plays a dominate role in weakening of stratospheric wave activity at the same month, and the effect of tropical SST change before September is negligible compared to that in September (The detailed evidences to address this issue are shown in the appendix).

~~6.~~7. Conclusions and Discussions

This study analyzes the trend of Antarctic stratospheric planetary wave activities in early austral spring since the early 2000s based on various reanalysis datasets and model simulations. Using the change-point method, we find that the Antarctic stratospheric wave activities in September have been weakening significantly since 2000, which means the intensified trend of wave activities noted in previous researches (Hu & Fu, 2009; Lin et al., 2009) are reversed after 2000 in early austral spring. Further analysis suggests that the weakening of stratospheric wave activities is related to the weakening of tropospheric wave sources in extratropical ~~Southern~~ southern ~~Hemisphere~~hemisphere, which is mainly contributed by the wave-1 component.

As the Antarctic ozone also shows clear shift around the 2000, we firstly examine the impact of ozone recovery on Antarctic stratospheric planetary wave activity. Our simulation results indicate that significant ozone recovery in lower stratosphere changes the atmospheric state for wave propagation to some extent, inducing a slight decrease of vertical wave flux over UTLS region in subpolar southern hemisphere. Meanwhile, the changes of wave activity in middle and upper stratosphere over subpolar region induced by ozone recovery are not significant. Therefore, the ozone recovery has minor contribution to the significant weakening of stratospheric planetary wave activity in September.

~~Moreover,~~ EOF analysis and correlation analysis indicate that the stratospheric wave activities in early austral spring during 2000-2017 are related to PC2 of SST over 20°N-70°S (i.e., the SHtrop region). The corresponding EOF2 mode also shows a good~~great~~ similarity to the spatial pattern of SST trend, suggesting that the weakening of stratospheric wave activities is connected to the trend of SST in SHtrop region. Meanwhile, the linkage between the SST trend in NH region and the weakening of stratospheric wave activities is weak. ~~Finally, t~~The model simulations also support ~~the conclusion~~ that the SST changes in SHtrop region lead to ~~the~~ a weakening of tropospheric wave sources and stratospheric wave activities. The contribution of SST trend in tropical region to the weakening of stratospheric wave activities is larger than that in the extratropical southern hemisphere. However, the response of tropospheric wave sources and stratospheric wave activities to SST trend in NH region is not significant. The contribution of SST trend over SHtrop region to the weakening of stratospheric wave activities is about 34%. Finally, both reanalysis datasets and numerical simulations indicate that the Brewer-Dobson circulation related to stratospheric wave activity has also been weakening in early austral spring since 2000, which is also attributed to the changes of September SST in tropics and extratropical southern hemisphere.

Although many researchers claimed that the climate transition around 2000 in southern hemisphere is related to ozone depletion and recovery (e.g., Barnes et al., 2013; Banerjee et al., 2020), there is no contradiction between our results and these previous studies. Firstly, the southern hemisphere tropospheric circulation (i.e., the SAM index, the tropospheric jet position and the Hadley cell edge) shifts related to ozone changes in these previous studies basically occurred in austral summer (e.g., Son et al, 2008; Thompson et al., 2011; Barnes et al, 2013; Banerjee et al., 2020). These tropospheric circulation changes are induced by downward coupling of circulation anomalies in the stratosphere (e.g., Thompson et al., 2011) during October and November, when solar radiation covers the entire Antarctic and causes heating effects. However, the Antarctic stratospheric circulation response to ozone variation in September is not as strong as that in October or November (e.g., Thompson et al., 2011, Figs. 1b, d) because solar radiation can only reach part of Antarctic stratosphere during a majority period of September. This implies that the response of atmospheric state in September to Antarctic stratospheric ozone change is not significant. Secondly, the FWSC component used in this study is an atmospheric module with prescribed SST and forcing gases. Therefore, our model results only indicate that the weakening of stratospheric wave activity can be attributed to SST changes, while the impact of ozone change in middle and low latitudes on SST cannot be determined based on these simulations. Whether the transition signal of Antarctic stratospheric ozone is stored in the ocean needs more efforts to explore. This is an issue beyond the scope of this study and further investigation is necessary by using a fully coupled earth system model.

The southern hemisphere stratospheric wave activity trend from the early 1980s to the early 2000s has been examined by Hu and Fu (2009) and hence is not analyzed in the present study. Wang and Waugh (2012) used stratosphere-resolving chemistry-climate model forced by time-varying factors to evaluate the trends of stratospheric temperature, residual circulation as well as wave activity during recent decades, and the trend of cumulative eddy heat flux shown in their paper is not significant (Fig. 6 in Wang and Waugh (2012)). In addition, Polvani et al. (2018) used time-varying ODSs to simulate Brewer-Dobson circulation and attained obvious trend transition around 2000. Their simulations cover from 1960s to 2080s. The significance of simulated trend may be related to model performance and the length of simulating period. As the period we focus is relatively short and our purpose is attribution rather than generating a real trend, we perform the ensemble time-slice experiments in this study, which are also used in many other previous researches (e.g., Hu et al., 2018; Kang et al., 2011; Zhang et al., 2016) to attribute trends in the atmosphere. In addition, most of the current climate models cannot generate a realistic wave activity trend as waves in the atmosphere are linked with various processes and factors (e.g., Baldwin & Dunkerton, 2005; Garcia & Randel, 2008; Labitzke, 2005; Shindell et al., 1999; Shu et al., 2013; Xie et al., 2008).

The question that remains answered is whether the ozone recovery trend also contributes to the weakening of stratospheric wave activities in September since the early 2000s. As described in Section 2, a control experiment (O3ctrl) forced by climatological ozone and a sensitive experiment forced by the linear increment of global ozone in September during 2001-2017 are conducted to address the above question. The pattern of ozone forcing field is similar to its trend pattern (Figs. S4c, d; Fig. S5). We choose the period of 2001-2017 because we notice that the ozone recovery trend derived from MERRA-2 in September with the beginning year of 2000 is not significant (Fig. S4a, b). Meanwhile, as the SSW in 2002 induces poleward transport of large amounts of ozone, the data in 2002 are removed when linear increments are calculated. Other details about these two experiments have been given in Section 2 and

Table 2. The simulated results indicate that there is no significant response of wave flux (Fig. 11a, d) as well as its Fourier decomposed components (Fig. 11b, c) over southern hemisphere subpolar region in the stratosphere, suggesting that the prescribed ozone recovery is incapable of inducing the weakening of stratospheric wave activities.

Many researchers claimed that the climate transition around 2000 in the southern hemisphere is related to ozone depletion and recovery (e.g., Barnes et al., 2013; Banerjee et al., 2020). Note that there is no contradiction between our results and these previous studies. Firstly, the southern hemisphere tropospheric circulation (i.e., the SAM index, the tropospheric jet position and the Hadley cell edge) transition related to ozone depletion and recovery reported in these previous studies basically occurred in austral summer (e.g., Son et al., 2008; Thompson et al., 2011; Barnes et al., 2013; Banerjee et al., 2020). These tropospheric circulation transitions are induced by downward coupling of circulation anomalies in the stratosphere (e.g., Thompson et al., 2011) during October and November, when solar radiation covers the entire Antarctic and causes radiative heating effects. However, we focus on September in the present study. The Antarctic stratospheric circulation response to ozone variation in September is not as strong as that in October or November (e.g., Thompson et al., 2011, Fig. 1b, d) because solar radiation can only reach part of the Antarctic stratosphere during a majority period of September. This fact implies that the response of wave propagation environment in the Antarctic stratosphere to ozone trend is also not significant (Fig. S6). Secondly, the FWSC component used in this study is an atmospheric module with prescribed SST and gases. Therefore, the model results only indicate that the weakening of stratospheric wave activities can be attributed to SST trends, while the impact of ozone depletion and recovery trend in the tropics and mid-latitudes on the shift of SST trend pattern cannot be determined based on the model simulations. This is an issue beyond the scope of this study and further investigation is necessary using a fully coupled earth system model.

In addition, the reanalysis datasets show that the Brewer-Dobson circulation related to wave activities in the stratosphere weakened significantly in early austral spring during 2000-2017 (Fig. 12b), which is contrary to the intensified trend during 1980-2000 (Fig. 12a). The transition of BDC around 2000 is believed to be associated with ozone depletion and recovery (e.g., Polvani et al., 2017; Polvani et al., 2018). However, our modeling results suggest that the SST trend is responsible for the weakening of BDC in September since 2000 (Fig. 12d, e, f), The response of BDC to ozone recovery is not significant (Fig. 12c), especially for the branch near the Antarctic. These results indicate that the SST trend should be taken into consideration when exploring the mechanism for the climate transition in the southern hemispheric stratosphere around 2000.

Data availability:

The ERA-Interim is available at: https://apps.ecmwf.int/datasets/data/interim-full-daily/levtype=sfc/. The MERRA-2 is available at: https://disc.gsfc.nasa.gov/datasets?keywords=%22MERRA-2%22&page=1&source=Models%2FAnalyses%20MERRA-2. The JRA-55 is available at: https://jra.kishou.go.jp/JRA-55/index_en.ht

带格式的: 缩进: 首行缩进: 2 字符, 允许文字在单词中间换行

ml#download. The NCEP-2 is available at: http://www.cpc.ncep.noaa.gov/products/wesley/reanalysis2/. The ERSST v5 dataset is available at: https://www1.ncdc.noaa.gov/pub/data/cmb/ersst/v5/netcdf/. The observations of TCO from SBUV v8.6 satellite dataset are available at: https://acd-ext.gsfc.nasa.gov/Data_services/merged/data/sbuv_v86_mod.int_lyr.70-18.za.r7.txt. The unfiltered IPO index derived from ERSST v5 dataset is available at: https://psl.noaa.gov/data/timeseries/IPOTPI/tpi.timeseries.ersstv5.data.

Author contributions:

Yihang Hu conducted experiments, produced figures and tables, organized and wrote the manuscript. Wenshou Tian, Jiankai Zhang and Tao Wang contributed to revise the manuscript. Mian Xu helped to design experiments.

Competing interests:

The authors declare that they have no competing interest.

Acknowledgements:

This work is supported by the National Natural Science Foundation of China (41630421 and 42075062). We thank Institute Pierre Simon Laplace (IPSL), NCEP and NCAR~~, National Aeronautics and Space Administration (NASA)~~ and Japan Meteorological Agency (JMA) for providing ERA-Interim, NCEP-2~~, MERRA-2~~ and JRA-55 datasets. We thank National Aeronautics and Space Administration (NASA) for providing MERRA-2 dataset and SBUV v8.6 satellite dataset. We thank National Oceanic and Atmospheric Administration (NOAA) for providing ERSST v5 dataset and IPO index. We also thank the scientific team at NCAR for providing CESM-1 model.

带格式的: 字体: 非加粗
带格式的: 字体: 非加粗
带格式的: 字体: 非加粗
带格式的: 字体: 非加粗
带格式的: 字体: 非加粗
带格式的: 缩进: 首行缩进: 2 字符
带格式的: 字体: 非加粗
带格式的: 缩进: 首行缩进: 2 字符
带格式的: 字体: 非加粗

Finally, we thank the computing support provided by the Supercomputing Center and the College of Atmospheric Sciences, from Lanzhou University.

APPENDIX

Analysis of time lag for tropical SST affects Antarctic stratospheric wave activity

As stated in the Section 2, the tropical SST anomalies (the linear inecrements) in experiment ssttrop are also applied in July and August (Fig. S4) to avoid abrupt SST variations from month to month, and the two months are taken as spin-up time. Therefore, whether the SST forcing in July and August also contribute to the weakening of Antarctic stratospheric wave activity in September or not cannot be justified based on the experiment ssttrop only. Here, we performed an additional experiment ssttropAug without September SST anomalies (Fig. S4f) to clarify whether the weakening of Antarctic stratospheric wave activity is induced by the tropical SST trend at the same month. Like other numerical experiments described in Table 1, the ssttropAug also includes 100 ensemble members that run from July to September forced by the same initial conditions from the 21st year to the 120th year in July generated by free run. The detailed descriptions of ssttropAug and other relevant experiments in the manuscript are displayed together in the Table S1 for comparison. Figure S4 shows the applied global SST anomalies in ssttrop and ssttropAug from July to September.

The responses of tropospheric wave sources and stratospheric wave activities in ssttropAug are shown in Figs. S5a-c and Figs. S5d-f, respectively. Note that the

带格式的: 居中, 缩进: 首行缩进: 0 字符
带格式的: 字体: 四号
带格式的: 字体: 加粗
带格式的: 字体: 四号, 加粗
带格式的: 缩进: 首行缩进: 2 字符

anomalies of subpolar tropospheric geopotential height in September forced by changes in tropical SST in August does not superpose on their climatological patterns in an evident out-of-phase style (Figs. S5a-c). The anomaly of wave-1 component of geopotential height shows a slight in-phase overlap with its climatology over subpolar region (Fig. S5b). Accordingly, the responses of stratospheric wave activities over subpolar of southern hemisphere are not significant (Figs. S5d-f). The results here suggest that, the decrease of September vertical wave flux induced by SST changes in August is negligible comparing to that in the experiment with anomalous SST forcing in September (Figs. S5g), and the tropical SST trend in September plays a dominate role in weakening of stratospheric wave activity at the same month.

Furthermore, we also use a linear barotropic model (LBM) (e.g., Shaman & Tziperman, 2007; Shaman & Tziperman, 2011) to quantify the time scale for propagation of tropical anomalies to high latitudes. The LBM are developed to solve the barotropic vorticity equation, which is given as Eq. (A1):

$$J(\bar{\psi},\nabla^2\psi')+J(\psi',\nabla^2\bar{\psi}+f)+\alpha\nabla^2\psi'+K\nabla^4\nabla^2\psi'=R \qquad \text{(A1)}$$

where the Jacobian $J(A,B)$ is

$$J(A,B)=\frac{1}{r^2}\left(\frac{\partial A}{\partial\lambda}\frac{\partial B}{\partial\mu}-\frac{\partial A}{\partial\mu}\frac{\partial B}{\partial\lambda}\right) \qquad \text{(A2)}$$

the forcing function R is

$$R=-(f+\nabla^2\bar{\psi})D \qquad \text{(A3)}$$

ψ is the streamfunction, f is the Coriolis force, α is the Rayleigh coefficient, K

is the diffusion coefficient, λ is the longitude, $\mu = \sin(\theta)$, θ is the latitude, r is the earth's radius and D is the divergence.

We use the wave-1 component of streamfunction derived from ensemble mean of sstctrl as the background field. In LBM, the initial anomaly is given by the divergence. The divergence forcing field is limited in 40°E-140°W, 10°S-0° (Fig. S6) to ensure that the tropical initial anomaly of streamfunction superpose on its background field in an out-of-phase style. We set $D = -7.9 \times 10^{-7} \ s^{-1}$, which is the mean divergence over the forcing region. The LBM simulated streamfunction anomalies are shown in Figs. S7b-i. Note that the anomalies in tropics only take a few days to arrive the high latitudes in southern hemisphere. After about four days, a stable anti-phase superposition of streamfunction is well established in extratropical southern hemisphere (Figs. S7f-i). These results are supported by previous studies (e.g., Shaman & Tziperman, 2011), which also indicate that the horizontal propagation of anomaly in atmosphere takes a few days.

Previous studies also reported that it takes about 4 days for wave-1 to propagate from troposphere into stratosphere and 1-2 days for wave-2 (e.g., Randel, 1987). Thus, the tropical oceans affect the stratosphere at mid-high latitudes with a lag of several days. However, the SST forcing field applied in CESM is on monthly scale. It is reasonable to use September SST trend to drive and explain the trends of extratropical circulation and wave activity at the same month.

Reference

域代码已更改
域代码已更改
域代码已更改
域代码已更改
域代码已更改
带格式的: 缩进: 首行缩进: 2 字符, 行距: 2 倍行距
域代码已更改
带格式的: 行距: 2 倍行距
带格式的: 缩进: 首行缩进: 2 字符

Andrews, D. G., Holton, J. R., & Leovy, C. B.: Middle atmosphere dynamics, (p. 489), San Diego, Calif: Academic Press Inc, 1987.

Angell, J. K., & Free, M.: Ground-based observations of the slowdown in ozone decline and onset of ozone increase, J. Geophys. Res., 114(D7), D07303, https://doi.org/10.1029/2008JD010860, 2009.

~~Brewer, A. W.: Evidence for a world circulation provided by the measurements of helium and water vapour distribution in the stratosphere, Q. J. Roy. Meteor. Soc., 75(326), 351-363, https://doi.org/10.1002/qj.49707532603, 1949.~~

Baldwin, M., P., Dunkerton, T. J.: Stratospheric harbingers of anomalous weather regimes, Science. https://doi.org/10.1126/science.1063315, 2001.

Baldwin, M., P., Dunkerton, T., J.: The solar cycle and stratosphere-troposphere dynamical coupling. J. Atmos. Sol-Terr. Phy., 67(1-2), 71-82, https://doi.org/10.1016/j.jastp.2004.07.018, 2005.

Baldwin, M., Hirooka, T., O'Neill, A., Yoden, S., Charlton, A. J., Hio, Y., & Yoden, S.: Major stratospheric warming in the Southern Hemisphere in 2002: Dynamical aspects of the ozone hole split, SPARC Newsletter, 20, 24–26, 2003.

Banerjee, A., Fyfe, J. C., Polvani, L. M., Waugh D., Chang K. L.: A pause in Southern Hemisphere circulation trends due to the Montreal Protocol, Nature, 579(7800), 544–548, https://doi.org/10.1038/s41586-020-2120-4, 2020.

Birner, T., & Bönisch, H.: Residual circulation trajectories and transit times into the extratropical lowermost stratosphere, Atmos. Chem. Phys., 11(2), 817–827, https://doi.org/10.5194/acp-11-817-2011, 2011.

~~Barnes, E. A., Barnes, N. W., Polvani, L. M.: Delayed southern hemisphere climate change induced~~

by stratospheric ozone recovery, as projected by the cmip5 models, J. Climate, 27(2), 852-867, https://doi.org/10.1175/JCLI-D-13-00246.1, 2014

Bosilovich, M., Akella, S., Coy, L., Cullather, R., Draper, C., Gelaro, R. and Suarez, M.: MERRA-2: Initial Evaluation of the Climate, NASA Technical Report Series on Global Modeling and Data Assimilation, 43, 139, 2015.

Banerjee, A., Fyfe, J. C., Polvani, L. M., Waugh D., Chang K. L.: A pause in Southern Hemisphere circulation trends due to the Montreal Protocol, Nature, 579(7800), 544-548, https://doi.org/10.1038/s41586-020-2120-4, 2020.

Charney, J. G., & Drazin, P. G.: Propagation of planetary-scale disturbances from the lower into the upper atmosphere, J. Geophys. Res., 66(1), 83-109, https://doi.org/10.1029/JZ066i001p00083, 1961.

Dee, D. P., Uppala, S. M., Simmons, A. J., Berrisford, P., Poli, P., Kobayashi, S., et al.: The ERA-Interim reanalysis: Configuration and performance of the data assimilation system, Q. J. Roy. Meteor. Soc., 137(656), 553–597, https://doi.org/10.1002/qj.828, 2011.

Gillett, N. P., Allen, M. R., & Williams, K. D.: Modelling the atmospheric response to doubled CO2 and depleted stratospheric ozone using a stratosphere-resolving coupled GCM, Q. J. Roy. Meteor. Soc., 129(589), 947–966, https://doi.org/10.1256/qj.02.102, 2003.

Garcia, R. R., & Randel, W. J.: Acceleration of the brewer-dobson circulation due to increases in greenhouse gases, J. Atmos. Sci., 65(8), 2731-2739, https://doi.org/10.1175/2008JAS2712.1, 2008.

Gabriel, A., H. Körnich, Lossow, S., Peters, D. H. W., & Murtagh, D.: Zonal asymmetries in middle

带格式的: 缩进: 左侧: 0 厘米, 首行缩进: 0 厘米

atmospheric ozone and water vapour derived from odin satellite data 2001–2010, Atmos. Chem. and Phys., 11(18), 9865-9885, https://doi.org/10.5194/acp-11-9865-2011, 2011.

Garcia, R. R., & Randel, W. J.: Acceleration of the brewer-dobson circulation due to increases in greenhouse gases, J. Atmos. Sci., 65(8), 2731-2739. https://doi.org/10.1175/2008JAS2712.1, 2008.

Haigh, J. D., Blackburn, M., & Day, R.: The response of tropospheric circulation to perturbations in lower-stratospheric temperature, J. Climate, 18(17), 3672-3685. https://doi.org/10.1175/JCLI3472.1, 2005.

Haynes, P. H., M. E. McIntyre, T. G. Shepherd, C. J. Marks, and K. P. Shine.: On the "Downward Control" of Extratropical Diabatic Circulations by Eddy-Induced Mean Zonal Forces, J. Atmos. Sci., 48(4), 651–678, https://doi.org/10.1175/1520-0469(1991)048<0651:OTCOED>2.0.CO;2, 1991.

~~Haigh, J. D., Blackburn, M., & Day, R.: The response of tropospheric circulation to perturbations in lower-stratospheric temperature, J. Climate, 18(17), 3672-3685. https://doi.org/10.1175/JCLI3472.1, 2005.~~

Holton, J.: An introduction to dynamic meteorology, (p. 535), Elsevier Academic Pr., 2004.

~~Hu, Y., & Fu, Q.: Stratospheric warming in southern hemisphere high latitudes since 1979, Atmos. Chem. Phys., 9(13), 4329-4340, https://doi.org/10.5194/acp-9-4329-2009, 2009.~~

~~Hurwitz, M. M., Newman, P. A., Oman, L. D., & Molod, A. M.: Response of the antarctic stratosphere to two types of El niño events, J. Atmos. Sci., 68(4), 812-822. https://doi.org/10.1175/2011JAS3606.1, 2011.~~

~~Haarsma, R. J., & Selten, F.: Anthropogenic changes in the Walker circulation and their impact on~~

the extra-tropical planetary wavestructure in the Northern Hemisphere, Clim. Dynam., 39(7–8), 1781–1799, https://doi.org/10.1007/s00382-012-1308-1, 2012.

Huang, B., Peter W. Thorne, et. al.: Extended Reconstructed Sea Surface Temperature version 5 (ERSSTv5), Upgrades, validations, and intercomparisons, J. Climate, 30(20), 8179-8205, https://doi.org/10.1175/JCLI-D-16-0836.1, 2017.

Hu, D., Tian, W., Xie, F., Shu, J., Dhomse, S.: Effects of meridional sea surface temperature changes on stratospheric temperature and circulation, Adv. Atmos. Sci., 31, 888–900. https://doi.org/10.1007/s00376-013-3152-6, 2014.

Hu, D., Tian, W., Xie, F., Wang, C., Zhang, J.: Impacts of stratospheric ozone depletion and recovery on wave propagation in the boreal winter stratosphere, J. Geophys. Res-Atmos., 120(16), 8299-8317, https://doi.org/10.1002/2014JD022855, 2015.

Hu, D., Guan, Z., Tian, W., & Ren, R.: Recent strengthening of the stratospheric Arctic vortex response to warming in the central North Pacific, Nat. Commun., 9(1), 1697. https://doi.org/10.1038/s41467-018-04138-3, 2018.

Hu, D., Guo, Y., & Guan, Z.: Recent weakening in the stratospheric planetary wave intensity in early winter, Geophys. Res. Lett., 46(7), 3953-3962, https://doi.org/10.1029/2019GL082113, 2019.

Hurwitz, M. M., Newman, P. A., Oman, L. D., & Molod, A. M.: Response of the antarctic stratosphere to two types of El niño events, J. Atmos. Sci., 68(4), 812-822. https://doi.org/10.1175/2011JAS3606.1, 2011.

Hu, Y., & Fu, Q.: Stratospheric warming in southern hemisphere high latitudes since 1979, Atmos. Chem. Phys., 9(13), 4329-4340, https://doi.org/10.5194/acp-9-4329-2009, 2009.

带格式的: 字体: (默认) Times New Roman, 10 磅

~~Huang, B., Peter W. Thorne, et. al.: Extended Reconstructed Sea Surface Temperature version 5 (ERSSTv5), Upgrades, validations, and intercomparisons, J. Climate, 30(20), 8179-8205, https://doi.org/10.1175/JCLI-D-16-0836.1, 2017~~.

Ialongo, I., Sofieva, V., Kalakoski, N., Tamminen, J., & E. Kyrölä.: Ozone zonal asymmetry and planetary wave characterization during antarctic spring, Atmos. Chem. Phys., 12(5), 2603-2614, https://doi.org/10.5194/acp-12-2603-2012, 2012.

Kanamitsu, M., Ebisuzaki, W., Woollen, J., Yang, S. K., Hnilo, J. J., Fiorino, M., & Potter, G. L.: NCEP–DOE AMIP-II Reanalysis (R-2), B. Am. Meteorol. Soc., 83(11), 1631–1644. https://doi.org/10.1175/BAMS-83-11-1631, 2002.

Kang, S. M. , Polvani, L. M. , Fyfe, J. C. , & Sigmond, M.: Impact of polar ozone depletion on subtropical precipitation, Science, 332(6032), 951-954, https://doi.org/10.1126/science.1202131, 2011.

Kim, B. M., Son, S. W., Min, S. K., Jeong, J. H., Kim, S. J., Zhang, X., Shim, T., Yoon, J. H.: Weakening of the stratospheric polar vortex by Arctic sea-ice loss, Nat. Commun., 5(1), 4646, https://doi.org/10.1038/ncomms5646, 2014.

Kobayashi, S., Y. Ota, Y. Harada, A. Ebita, M. Moriya, H. Onoda, K. Onogi, H. Kamahori, C. Kobayashi, H. Endo, K. Miyaoka, and K. Takahashi,: The JRA-55 Reanalysis: General specifications and basic characteristics, J. Meteorol. Soc. of Jpn., 93(1), 5-48, https://doi.org/10.2151/jmsj.2015-001, 2015.

Kravchenko, V. O., Evtushevsky, O. M., Grytsai, A. V., Klekociuk, A. R., Milinevsky, G. P., and Grytsai, Z. I.: Quasi-stationary planetary waves in late winter Antarctic stratosphere

带格式的: 缩进: 左侧: 0 厘米, 首行缩进: 0 厘米

temperature as a possible indicator of spring total ozone, Atmos. Chem. Phys., 11(10), 28945–28967, https://doi.org/10.5194/acp-12-2865-2012, 2011.

Krzyścin, J. W.: Onset of the total ozone increase based on statistical analyses of global ground-based data for the period 1964 – 2008, Int. J. Climatol., 32(2), 240-246, https://doi.org/10.1002/joc.2264, 2012.

~~Kim, B. M., Son, S. W., Min, S. K., Jeong, J. H., Kim, S. J., Zhang, X., Shim, T., Yoon, J. H.: Weakening of the stratospheric polar vortex by Arctic sea-ice loss, Nat. Commun., 5(1), 4646, https://doi.org/10.1038/ncomms5646, 2014.~~

~~Kobayashi, S., Y. Ota, Y. Harada, A. Ebita, M. Moriya, H. Onoda, K. Onogi, H. Kamahori, C. Kobayashi, H. Endo, K. Miyaoka, and K. Takahashi,: The JRA-55 Reanalysis: General specifications and basic characteristics, J. Meteorol. Soc. of Jpn., 93(1), 5-48, https://doi.org/10.2151/jmsj.2015-001, 2015.~~

Labitzke, K.: On the solar cycle-QBO relationship: A summary. J. Atmos. Sol-Terr. Phy., 67(1-2), 45-54, https://doi.org/10.1016/j.jastp.2004.07.016, 2005.

Lin, P., Fu, Q., Solomon, S., & Wallace, J. M.: Temperature trend patterns in southern hemisphere high latitudes: novel indicators of stratospheric change, J. Climate, 22(23), 6325-6341. https://doi.org/10.1175/2009JCLI2971.1, 2009.

~~Li, S.: The influence of tropical indian ocean warming on the southern hemispheric stratospheric polar vortex, Sci. China. Ser. D., 52(3), 323-332, https://doi.org/10.1007/s11430-009-0029-8, 2009.~~

Lin, P., Fu, Q., & Hartmann, D.: Impact of tropical ~~sst~~ SST on stratospheric planetary waves in the southern hemisphere, J. Climate, 25(14), 5030-5046. https://doi.org/10.1175/JCLI-D-11-

00378.1, 2012.

Li, S.: The influence of tropical indian ocean warming on the southern hemispheric stratospheric polar vortex, Sci. China. Ser. D., 52(3), 323–332, https://doi.org/10.1007/s11430-009-0029-8, 2009.

Li, Y., & Tian, W.: Different impact of central pacific and eastern pacific el El niñno on the duration of sudden stratospheric warming, Adv. Atmos. Sci., 34(06), 771-782. https://doi.org/10.1007/s00376-017-6286-0, 2017.

Li, Y., Tian, W., Xie, F., Wen, Z., Zhang, J., Hu, D., & Han, Y.: The connection between the second leading mode of the winter North Pacific sea surface temperature anomalies and stratospheric sudden warming events, Clim. Dynam., 51(1-2), 581 – 595. https://doi.org/10.1007/s00382-017-3942-0, 2018.

Lim, E. P., Hendon, H. H., Boschat, G. Hudson, D., Thompson, D. J., Dowdy, A., J., Arblaster, J. M.: Australian hot and dry extremes induced by weakenings of the stratospheric polar vortex, Nat. Geosci., 12, 896–901, https://doi.org/10.1038/s41561-019-0456-x, 2019.

Marsh, D. R., Mills, M. J., Kinnison, D. E., Lamarque, J. F., Calvo, N., & Polvani, L. M.: Climate change from 1850 to 2005 simulated in CESM1 (WACCM), J. Climate, 26(19), 7372-7391. https://doi.org/10.1175/JCLI-D-12-00558.1, 2013.

Nishii, K. and Nakamura, H.: Tropospheric influence on the diminished Antarctic ozone hole in September 2002, Geophys. Res. Lett., 31(16), L16103, https://doi.org/10.1029/2004GL019532, 2004.

Neale, R. B., Richter, J., Park, S., Lauritzen, Lauritzen, P. H., Vavrus, S. J., Rasch, P. J., & Zhang, M.:The mean climate of the community atmosphere model (cam4) in forced sst and fully coupled experiments, J. Climate, 26(14), 5150-5168, https://doi.org/10.1175/JCLI-D-12-00236.1, 2013.

Newman, P. A., & Nash, E. R.: The unusual Southern Hemisphere stratosphere winter of 2002, J. Atmos. Sci., 62(3), 614–628. https://doi.org/10.1175/JAS-3323.1, 2005.

Nishii, K. and Nakamura, H.: Tropospheric influence on the diminished Antarctic ozone hole in September 2002, Geophys. Res. Lett., 31(16), L16103, https://doi.org/10.1029/2004GL019532, 2004.

Neale, R. B., Richter, J., Park, S., Lauritzen, Lauritzen, P. H., Vavrus, S. J., Rasch, P. J., & Zhang, M.:The mean climate of the community atmosphere model (cam4) in forced sst and fully coupled experiments, J. Climate, 26(14), 5150-5168, https://doi.org/10.1175/JCLI-D-12-00236.1, 2013.

Polvani, L. M., & Bellomo, K.: The key role of ozone depleting substances in weakening the walker circulation in the second half of the 20th century, J. Climate, 32(5), 1411-1418. https://doi.org/10.1175/JCLI-D-17-0906.1, 2013.

Polvani, L. M., Wang, L., Aquila, V., & Waugh, D. W.: The impact of ozone depleting substances on tropical upwelling, as revealed by the absence of lower stratospheric cooling since the late 1990s, J. Climate, 30(7), 2523-2534. https://doi.org/10.1175/JCLI-D-16-0532.1, 2017.

Polvani, L. M., Abalos, M., Garcia, R., Kinnison, D., & Randel, W. J.: Significant weakening of Brewer-Dobson circulation trends over the 21st century as a consequence of the Montreal Protocol, Geophys. Res. Lett., 45(1), 401–409, https://doi.org/10.1002/2017GL075345, 2018.

Randel, W. J.: A study of planetary waves in the southern winter troposphere and stratosphere. Part

I: Wave structure and vertical propagation, J. Atmos. Sci., 44(6), 917-935, 1987.

Randel, W. J., & Wu, F.: Cooling of the arctic and antarctic polar stratospheres due to ozone depletion, J. Climate, 12(5), 1467-1479. https://doi.org/10.1175/1520-0442(1999)012<1467:COTAAA>2.0.CO;2, 1999.

Shaman, J., & Tziperman, E.: An atmospheric teleconnection linking ENSO and southwestern European precipitation, J. Climate., 24(1), 124-139, https://doi.org/10.1175/2010JCLI3590.1, 2011.

Shaman, J., & Tziperman, E.: Summertime ENSO-North African-Asian Jet teleconnection and implications for the Indian monsoons, Geophys. Res. Lett., 34(11), L11702, https://doi.org/10.1029/2006GL029143, 2007.

Shen, X., Wang, L., & Osprey, S.: The southern hemisphere sudden stratospheric warming of september 2019, Sci. Bull., 65(21), 1800-1802. https://doi.org/10.1016/j.scib.2020.06.028, 2020a.

Shen, X., Wang, L., & Osprey, S.: Tropospheric forcing of the 2019 antarctic sudden stratospheric warming, Geophys. Res. Lett., 47(20), e2020GLO89343, https://doi.org/10.1029/2020GL089343, 2020b.

Shindell, D., T., Miller, R., L., Schmidt, G., A., & Pandolfo, L.: Simulation of recent northern winter climate trends by greenhouse-gas forcing, Nature, 399(6735), 452-455, https://doi.org/10.1038/20905, 1999.

Shirley, D., Stanley, W., & Daniel, C.: Statistics for Research (Third Edition), (p. 627), Hoboken, New Jersey: John Wiley & Sons Inc., 2004.

Shu, J., Tian, W., Hu, D., Zhang, J., Shang, L., Tian, Hu., & Xie, F.: Effects of the quasi-biennial oscillation and stratospheric semi-annual oscillation on tracer transport in the upper stratosphere. J. Atmos. Sci., 70(5), 1370-1389, https://doi.org/10.1175/JAS-D-12-053.1, 2013.

Simpson, I. R., Blackburn, M., & Haigh, J. D.: The role of eddies in driving the tropospheric response to stratospheric heating perturbations, J. Atmos. Sci., 66(5), 1347-1365, https://doi.org/10.1175/2008JAS2758.1, 2009.

Solomon, S., Ivy, D. J., Kinnison, D., Mills, M. J., Neely, R. R., & Schmidt, A.: Emergence of healing in the antarctic ozone layer, *Science*, 353(6296), 269-274, https://doi.org/10.1126/science.aae0061, 2016.

Solomon, S.: Stratospheric ozone depletion: a review of concepts and history, Rev. Geophys., 37(3), 275-316, https://doi.org/10.1029/1999RG900008, 1999.

Son, S. W., Han, B. R., Garfinkel, C. I., Seo-Yeon, K., Rokjin, P., & Luke, A. N., et al.: Tropospheric jet response to antarctic ozone depletion: an update with chemistry-climate model initiative (CCMI) models, Environ. Res. Lett., 13(5), 054024-. https://doi.org/10.1088/1748-9326/aabf21, 2018.

Son, S. W., P. G. Edwin, K. H. Seo,: The impact of stratospheric ozone recovery on the Southern Hemisphere westerly jet, Science, 320(5882),: 1486-1489, https://doi.org/10.1126/science.1155939, 2008.

Susan, E., S., Douglass, A. R., Damon, M. R.: Why do antarctic ozone recovery trends vary?, J. Geophys. Res.-Atmos., 124(15), 8837-8850. https://doi.org/10.1029/2019JD030996, 2019.

Swart, N. C. & Fyfe, J. C.: Observed and simulated changes in the Southern Hemisphere surface westerly wind-stress, Geophys. Res. Lett., 39(16), L16711,

带格式的: 超链接, 字体: (默认) Times New Roman, 字体颜色: 文字 1

带格式的: 缩进: 左侧: 0 厘米, 悬挂缩进: 2 字符, 首行缩进: -2 字符

https://doi.org/10.1029/2012GL052810, 2012.

Solomon, S., Ivy, D. J., Kinnison, D., Mills, M. J., Neely, R. R., & Schmidt, A.: Emergence of healing in the antarctic ozone layer, *Science*, 353(6296), 269-274, https://doi.org/10.1126/science.aae0061, 2016.

Son, S. W., Han, B. R., Garfinkel, C. I., Seo-Yeon, K., Rokjin, P., & Luke, A. N., et al.: Tropospheric jet response to antarctic ozone depletion: an update with chemistry-climate model initiative (CCMI) models, Environ. Res. Lett., 13(5), 054024-. https://doi.org/10.1088/1748-9326/aabf21, 2018.

Susan, E., S., Douglass, A. R., Damon, M. R.: Why do antarctic ozone recovery trends vary?, J. Geophys. Res.-Atmos., 124(15), 8837-8850. https://doi.org/10.1029/2019JD030996, 2019.

Shen, X., Wang, L., & Osprey, S.: The southern hemisphere sudden stratospheric warming of september 2019, Sci. Bull., 65(21), 1800-1802. https://doi.org/10.1016/j.scib.2020.06.028, 2020a

Shen, X., Wang, L., & Osprey, S.: Tropospheric forcing of the 2019 antarctic sudden stratospheric warming, Geophys. Res. Lett., 47(20), e2020GLO89343, https://doi.org/10.1029/2020GL089343, 2020b.

Thompson, D., Solomon, S., Kushner, P. England, M., Grise, K. M., Karoly, D. J.: Signatures of the Antarctic ozone hole in Southern Hemisphere surface climate change, Nat. Geosci., 4, 741–749. https://doi.org/10.1038/ngeo1296, 2011.

Tian, W., Li, Y., Xie, F., Zhang, J., Chipperfield, M., & Feng, W., Hu, Y., Zhao, S., Zhou, X., Zhang, Y. & Ma, X.: The relationship between lower-stratospheric ozone at southern high latitudes and sea surface temperature in the east Asian marginal seas in austral spring, Atmos. Chem.

Phys., 17(11), 6705-6722. https://doi.org/10.5194/acp-17-6705-2017, 2017.

Trenberth, K. E., & Fasullo, J. T.: An apparent hiatus in global warming?, Earth's Future, 1(1), 19–32, https://doi.org/10.1002/2013EF000165, 2013.

~~Tian, W., Li, Y., Xie, F., Zhang, J., Chipperfield, M., & Feng, W., Hu, Y., Zhao, S., Zhou, X., Zhang, Y. & Ma, X.: The relationship between lower-stratospheric ozone at southern high latitudes and sea surface temperature in the east Asian marginal seas in austral spring, Atmos. Chem. Phys., 17(11), 6705-6722. https://doi.org/10.5194/acp-17-6705-2017, 2017.~~

Wang, T., Tian, W., Zhang, J., Xie, F., Zhang, R., Huang, J. & Hu, D.: Connections between Spring Arctic Ozone and the Summer Circulation and Sea Surface Temperatures over the Western North Pacific, J. Climate, 33(7): 2907–2923, https://doi.org/10.1175/JCLI-D-19-0292.1, 2020.

WMO.: Scientific assessment of ozone depletion: 2010, World Meteorological Organization/United Nations Environment Programme Rep. 52, 516 pp, 2011.

WMO.: Antarctic ozone hole is smallest on record, World Meteorological Organization. Accessed October 2019 at https://public.wmo.int/en/media/news/antarctic-ozone-hole-smallest-record, 2019.

Xia, Y., Xu, W., Hu, Y., & Xie, F.: Southern-hemisphere high-latitude stratospheric warming revisit, Clim. Dynam., 54(3): 1671-1682. https://doi.org/10.1007/s00382-019-05083-7, 2020.

Xie, F., Tian, W., & Chipperfield, M., P.: Radiative effect of ozone change on stratosphere-troposphere exchange. J. Geophys. Res., 113, D00B09, https://doi.org/10.1029/2008JD009829, 2008

带格式的: 字体颜色: 文字 1

Xie, F., Zhang, J., Huang, Z., Lu, J., & Sun, C.: An estimate of the relative contributions of sea surface temperature variations in various regions to stratospheric change, J. Climate, 33(12), 4994-5011, https://doi.org/10.1175/JCLI-D-19-0743.1, 2020.

Yamazaki, Y., Matthias, V., Miyoshi, Y., Stolle, C., Siddiqui, T., Kervalishvili, G., et al.: September 2019 Antarctic sudden stratospheric warming: Quasi-6-day wave burst and ionospheric effects, Geophys. Res. Lett., 47(1), e2019GL086577. https://doi.org/10.1029/2019GL086577, 2020.

Zhang, J., Tian, W., Xie, F., Tian, H., Luo, J., Zhang, J., Liu, W., Dhomse, S.: Climate warming and decreasing total column ozone over the tibetan plateau during winter and spring, Tellus B., 66(1), https://doi.org/10.3402/tellusb.v66.23415, 2014.

Zhang, J., Tian, W. , Chipperfield, M. P. , Xie, F. , & Huang, J.: Persistent shift of the arctic polar vortex towards the eurasian continent in recent decades, Nat. Clim. Change. 6, 1094–1099. https://doi.org/10.1038/nclimate3136, 2016.

~~Zhang, P., Wu, Y. & Smith, K. L.: Prolonged effect of the stratospheric pathway in linking Barents–Kara Sea sea ice variability to the midlatitude circulation in a simplified model, Clim. Dynam. 50(17), 527–539. https://doi.org/10.1007/s00382-017-3624-y, 2018.~~

Zhang, J., Tian, W., Xie, F., Sang, W., Guo, D., Chipperfield, M., Feng, W., Hu, D.: Zonally asymmetric trends of winter total column ozone in the northern middle latitudes, Clim. Dynam., 52(7-8), 4483-4500, https://doi.org/10.1007/s00382-018-4393-y, 2019a.

Zhang, P., Wu, Y. & Smith, K. L.: Prolonged effect of the stratospheric pathway in linking Barents–Kara Sea sea ice variability to the midlatitude circulation in a simplified model, Clim. Dynam. 50(17), 527–539. https://doi.org/10.1007/s00382-017-3624-y, 2018.

Zhang, R., Tian, W., Zhang, J., Huang, J., & Xu, M.: The corresponding tropospheric environments during downward-extending and nondownward-extending events of stratospheric northern annular mode anomalies, J. Climate, 32(6), 1857-1873, https://doi.org/10.1175/JCLI-D-18-0574.1, 2019b.

Table 1. Configurations of experiments for SST trends.

Experiments	Descriptions
sstctrl	Control run. Seasonal cycle of monthly mean global SST data over 1980-2000 is derived from the ERSST v5 dataset. Fixed values of ozone greenhouse gases and aerosol fields in 2000 are used.
sstNH	As in sstctrl, but with linear increments of SST in September over 2000-2017 in NH (20°N-70°N). The applied global SST anomalies are shown in Fig. 7a.
sstSH	As in sstctrl, but with linear increments of SST in September over 2000-2017 in SH (20°S-70°S). The applied global SST anomalies are shown in Fig. 7b.
ssttrop	As in sstctrl, but with linear increments of SST in September over 2000-2017 in the tropics (20°S-20°N). The applied global SST anomalies are shown in Fig. 7c.
sstSHtrop	As in sstctrl, but with linear increments of SST in September over 2000-2017 in SHtrop (20°N-70°S). The applied global SST anomalies are shown in Fig. 7d.

Table 2. Configurations of experiments for the ozone recovery trend.

Experiments	Descriptions

O3ctrl	Control run. The seasonal cycle of monthly averaged global SST data over 1980-2000 is derived from ERSST v5 dataset. The seasonal cycle of monthly mean three-dimensional global ozone over 1980-2000 is derived from MERRA-2 dataset. The GHGs and aerosol fields are specified to be fixed values in 2000.
O3sen	As in O3ctrl, but superposed with linear increments of global ozone in September over 2001-2017. The ozone data in 2002 are removed when the linear increments are calculated. The applied ozone anomalies in Southern Hemisphere are shown in Fig. S5.

Table 3. Correlations of stratospheric vertical wave flux time series (area-weighted from 100 hPa to 30 hPa over 70°S-50°S) between different reanalysis dataset.

	ERA-Interim	JRA-55	MERRA-2	NCEP-2
ERA-Interim	1.00 (p=0.00)	0.99 (p<0.01)	0.98 (p<0.01)	0.93 (p<0.01)
JRA-55		1.00 (p=0.00)	0.98 (p<0.01)	0.93 (p<0.01)
MERRA-2			1.00 (p=0.00)	0.94 (p<0.01)
NCEP-2				1.00 (p=0.00)

~~**Figure captions:**~~

~~**FIG. 1.** Trends of southern hemisphere (a, d) stratospheric E-P flux (arrows, units of horizontal and vertical components are 10^5 and 10^3 kg·s^{-2} per year, respectively) and its divergence (shadings) with their (b, e) wave-1 components and (c, f) wave-2 components over (a, b, c) 1980-2000 and (d, e, f) 2000-2017 in September derived from MERRA-2 dataset. The stippled regions indicate the trend of E-P flux divergence significant at/above the 90% confidence level. The green contours from outside to inside (corresponding to p=0.1, 0.05) indicate the trend of vertical E-P flux significant~~

at the 90% and 95% confidence level, respectively.

FIG. 2. (a) The mean time series (solid line) and piecewise (during 1980-2000 and 2000-2018) linear regressions (dashed lines) of vertical E-P flux area-weighted from 100 hPa to 30 hPa over 70°S-50°S in September during 1980-2018 derived from ERA-Interim (yellow), MERRA-2 (blue), JRA-55 (red) and NCEP-2 (green). Figure (b) is the same as Figure (a), except for that the data in 2002 are removed. (c, d, e, f) The trends (dots) and uncertainties (error bars) calculated during various periods using the change-point method with different beginning and ending years (titles). Circles and squares in Figures (c, d, e, f) represent positive trends from beginning years to change-point years (x-axes) and negative trends from change-point years to ending years, respectively. Different colors of dots and error bars in Figures (c, d, e, f) correspond to colors in Figure (a), which represent trends and uncertainties derived from different datasets. The long and short error bars in same color reflect the 95% and 90% confidence intervals calculated by two-tailed t test. The error bar is omitted when the significance of trend is lower than corresponding confidence level. Negative trends and corresponding uncertainties with the beginning change-point years after 2005 are also omitted, since the trend value shows large fluctuation with shortening of time series. Figures (g, h, i, j) are the same as Figures (c, d, e, f), except that the data in 2002 are removed when calculating trends and uncertainties.

FIG. 3. Trends (shadings) and climatological distributions (contours with an interval of 20 gpm, positive and negative values are depicted by solid and dashed lines respectively, zeroes are depicted by thick solid lines) of southern hemispheric (a) 500

hPa geopotential height zonal deviations with their (b) wave-1 component and (c) wave-2 component in September during 2000–2017 derived from MERRA-2 dataset. Trends of southern hemispheric (d) tropospheric E-P flux (arrows, units of horizontal and vertical components are 3×10^{5} and 3×10^{3} kg s^{-2} per year, respectively) and its vertical component (shading) with their (e) wave-1 component and (f) wave-2 component in September during 2000–2017 derived from MERRA-2 dataset. The stippled regions represent the trend significant at/above the 90% confidence level.

FIG. 4. Trends of SST in September over (a) 1980-2000 and (b) 2000-2017 derived from ERSST v5 dataset. The stippled regions represent the trends significant at/above the 90% confidence level.

FIG. 5. Trend significance of the first three SST principal components (PCs) in (a) the extratropical southern hemisphere (SH, 70°S-20°S), (b) the tropics (TROP, 20°S-20°N), (c) the extratropical northern hemisphere (NH, 20°N-70°N), (d) the extratropical southern hemisphere and the tropics (SHtrop, 70°S-20°N), (e) the extratropical northern hemisphere and the tropics (NHtrop, 20°S-70°N), (f) the globe (70°S-70°N) and the corresponding (g, h, i, j, k, l) correlation significances between them and vertical E-P flux (Fz, area weighted from 100 hPa to 30 hPa over 70°S-50°S) during different beginning years (x-axes) and ending years (y-axes). The red and blue dots indicate positive and negative trend or correlation coefficient are significant, respectively. The black dots indicate the trends or correlation coefficients are not significant. The stars indicate that the trends and the corresponding correlation coefficients are both significant. Each panel is divided into three regions from bottom to top, corresponding

to the first, the second and the third principal components, respectively. The criterion to distinguish whether the trends and correlations are significant or not is the 90% confidence level.

FIG. 6. (a, b, c) The first three EOF patterns of SST in SHtrop region. (d, e, f) The original time series of the first three principle components (PCs, blue solid lines correspond to left inverted y-axes) and stratospheric vertical E-P flux (Fz, area-weighted from 100 hPa to 30 hPa over 70°S-50°S, red solid lines correspond to right y-axes) in September during 2000-2017. The blue and red dashed lines in (d, e, f) represent the linear regressions of PC time series and Fz time series, respectively. The meaning of (g, h, i) are the same as (d, e, f) correspondingly, except the detrended time series. The unbracketed and bracketed numbers in (g, h, i) represent the correlation coefficients between detrended PC time series and Fz time series and the corresponding p values calculated by two-tailed t test, respectively.

FIG. 7. Differences in SST forcing field between sensitive experiments ((a) sstNH; (b) sstSH; (c) ssttrop; (d) sstSHtrop) and the control experiment (sstctrl).

FIG. 8. Differences (shadings) of (a, d, g, j) 500 hPa geopotential height zonal deviations with their (b, e, h, k) wave-1 component and (c, f, i, l) wave-2 component between sensitive experiments ((a, b, c) sstNH; (d, e, f) sstSH; (g, h, i) ssttrop; (j, k, l) sstSHtrop) and the control experiment (sstctrl). The mean distributions (contours with an interval of 20 gpm, positive and negative values are depicted by solid and dashed lines respectively, zeroes are depicted by thick solid lines) of them are derived from the control experiment. The stippled regions represent the mean difference significant

at/above the 90% confidence level.

FIG. 9. Differences of (a, d, g, j) stratospheric E-P flux (arrows, units in horizontal and vertical components are 0.05×10^{7} and 0.05×10^{5} $kg\cdot s^{-2}$, respectively) and its divergence (shadings) with their (b, e, h, k) wave-1 component and (c, f, i, l) wave-2 component between sensitive experiments ((a, b, c) sstNH; (d, e, f) sstSH; (g, h, i) ssttrop; (j, k, l) sstSHtrop) and the control experiment (sstctrl). The stippled regions represent the mean differences of E-P flux divergence significant at/above the 90% confidence level. The green contours from outside to inside (corresponding to p=0.1, 0.05) represent the mean differences of vertical E-P flux significant at the 90% and 95% confidence levels, respectively.

FIG. 10. (a, b, c, d) Frequency distributions (pillars, blue for control experiment and orange for sensitive experiments) of vertical E-P flux (Fz, area-weighted from 200 hPa to 10 hPa over 70°S-50°S) and its 5-point low-pass filtered fitting curves (solid lines, blue for control experiment and red for sensitive experiments) derived from 100 ensemble members of the control experiment (sstctrl) and sensitive experiments ((a) sstNH; (b) sstSH; (c) ssttrop; (d) sstSHtrop), respectively. (e) Mean differences (grey pillars) and corresponding uncertainties (error bars) of Fz between sensitive experiments and the control experiment. The blue and red error bars reflect the 90% and 95% confidence levels calculated by two-tailed t test, respectively. The error bar is omitted when the significance of mean difference is lower than the corresponding confidence level.

FIG. 11. Differences of (a) stratospheric E-P flux (arrows, units in horizontal and

vertical components are 0.02×10^{7} and 0.05×10^{5} $kg\cdot s^{-2}$, respectively) and its divergence (shadings) with their (b) wave-1 component and (c) wave-2 component between the sensitive experiment (O3sen) and the control experiment (O3ctrl). The stippled regions represent the mean differences of E-P flux divergence significant at/above the 90% confidence level. The green contours from outside to inside (corresponding to p=0.1, 0.05) represent the mean differences of vertical E-P flux significant at the 90% and 95% confidence levels, respectively. (d) Frequency distributions (pillars, blue for O3ctrl and orange for O3sen) of vertical E-P flux (Fz, area-weighted from 200 hPa to 10 hPa over 70°S-50°S) and it 5-point low-pass filtered fitting curves (solid lines, blue for O3ctrl and red for O3sen) derived from 100 ensemble members.

FIG. 12. (a) Trends of southern hemispheric Brewer-Dobson circulation (arrows, units in horizontal and vertical components are 0.2×10^{-2} and 0.2×10^{-4} $m\cdot s^{-1}$ per year, respectively) and its stream function (shadings) in September during (a) 1980-2000 and (b) 2000-2017 derived from MERRA-2 dataset. Data in 2002 are removed when trends are calculated in Figure (b). (c) Differences of Brewer-Dobson circulation (arrows, units in horizontal and vertical components are 10^{-2} and 10^{-4} $m\cdot s^{-1}$, respectively) and its stream function (shadings) between the O3ctrl and O3sen. (d, e, f) Differences of Brewer-Dobson circulation and its stream function between the control experiment (sstctrl) and various sensitive experiments ((d) sstSH; (e) ssttrop; (f) sstSHtrop) with SST changes. The stippled regions represent the trends or differences of the stream function significant at/above the 90% confidence level. The green contours from outside to inside (corresponding to p=0.1, 0.05) represent the trends or differences of

~~the vertical components significant at the 90% and 95% confidence levels, respectively.~~

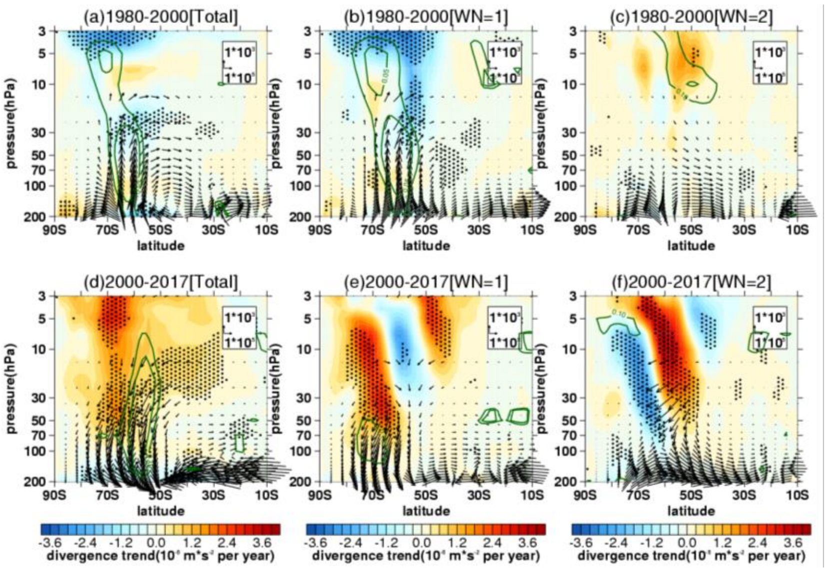

FIG. 1. Trends of southern hemisphere (a, d) stratospheric E-P flux (arrows, units of horizontal and vertical components are 10^5 and 10^3 kg·s^{-2} per year, respectively) and its divergence (shadings) with their (b, e) wave-1 components and (c, f) wave-2 components over (a, b, c) 1980-2000 and (d, e, f) 2000-2017 in September derived from MERRA-2 dataset. The stippled regions indicate the trend of E-P flux divergence significant at/above the 90% confidence level. The green contours from outside to inside (corresponding to p=0.1, 0.05) indicate the trend of vertical E-P flux significant at the 90% and 95% confidence level, respectively.

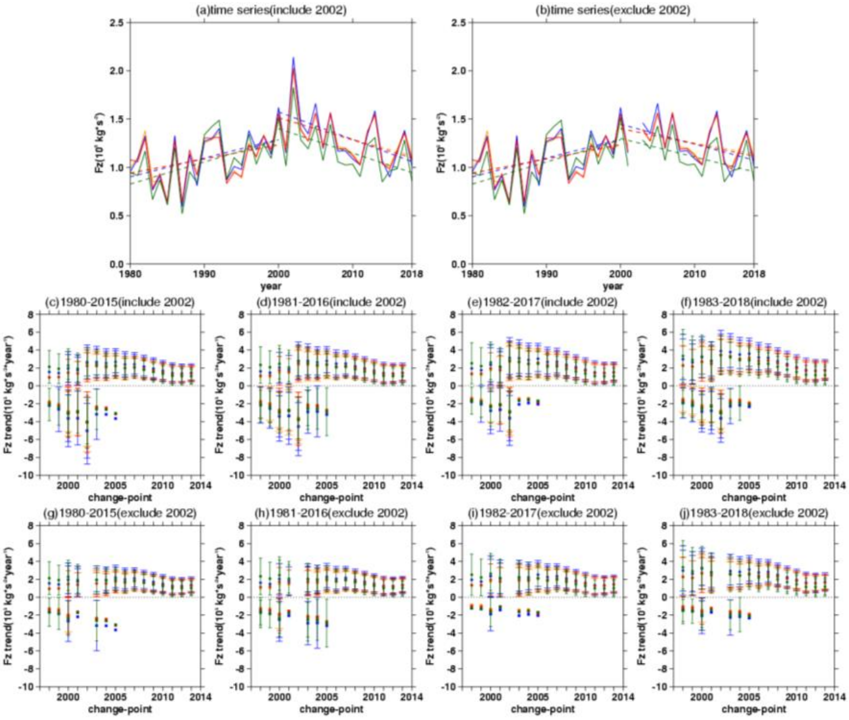
(a)time series(include 2002)
(b)time series(exclude 2002)
Fz(10⁷ kg*s⁻¹)
year
(c)1980-2015(include 2002)
(d)1981-2016(include 2002)
(e)1982-2017(include 2002)
(f)1983-2018(include 2002)
(g)1980-2015(exclude 2002)
(h)1981-2016(exclude 2002)
(i)1982-2017(exclude 2002)
(j)1983-2018(exclude 2002)
Fz trend(10⁷ kg*s⁻¹*year⁻¹)
change-point

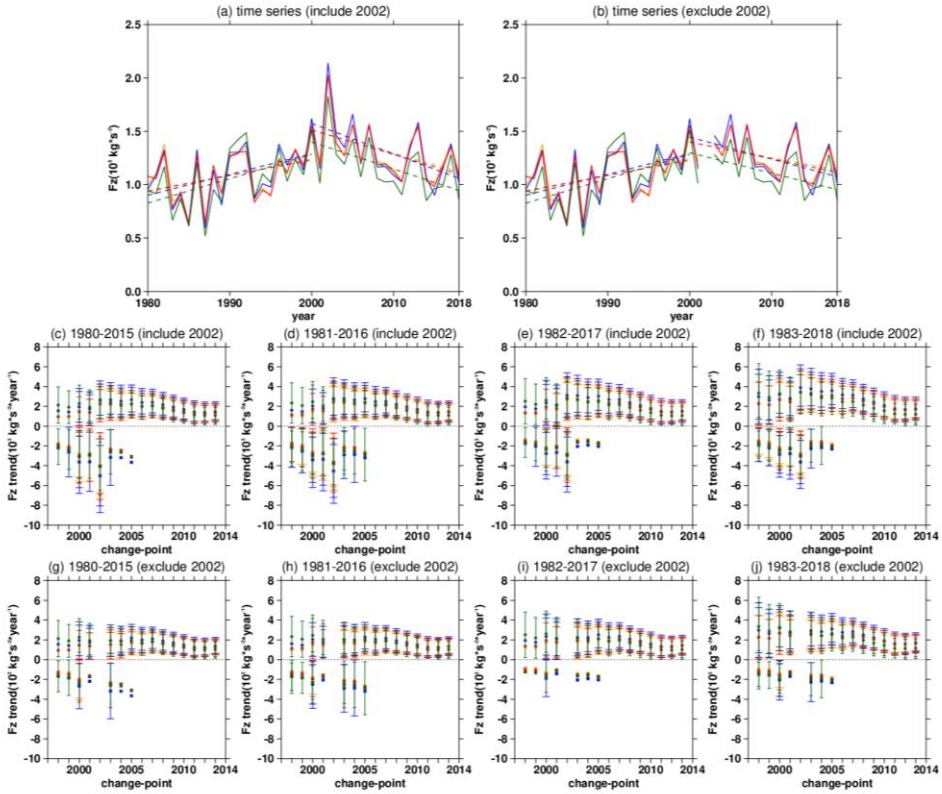

FIG. 2. (a) The mean time series (solid lines) and piecewise (during 1980-2000 and 2000-2018) linear regressions (dashed lines) of vertical E-P flux area-weighted from 100 hPa to 30 hPa over 70°S-50°S in September during 1980-2018 derived from ERA-Interim (yellow), MERRA-2 (blue), JRA-55 (red) and NCEP-2 (green). Figure (b) is the same as Figure (a), except for that the data in 2002 are removed. (c, d, e, f) The trends (dots) and uncertainties (error bars) calculated during various periods using the change-point method with different beginning and ending years (titles). Circles and squares in Figures (c, d, e, f) represent positive trends from beginning years to change-point years (x-axes) and negative trends from change-point years to ending years,

respectively. Different colors of dots and error bars in Figures (c, d, e, f) correspond to colors in Figure (a), which represent trends and uncertainties derived from different datasets. The long and short error bars in same color reflect the 95% and 90% confidence intervals calculated by two-tailed t test. The error bar is omitted when the significance of trend is lower than corresponding confidence level. Negative trends and corresponding uncertainties with the beginning change-point years after 2005 are also omitted, since the trend value shows large fluctuation with shortening of time series. Figures (g, h, i, j) are the same as Figures (c, d, e, f), except that the data in 2002 are removed when calculating trends and uncertainties.

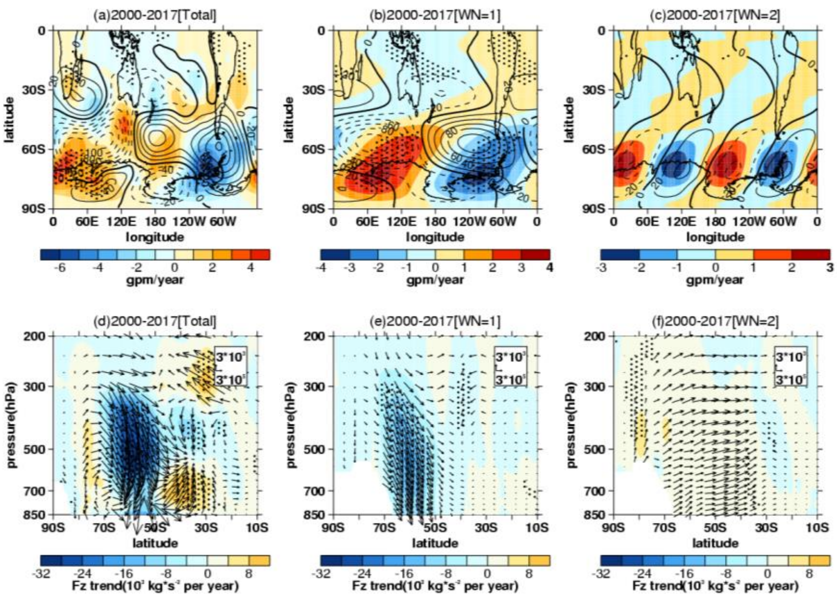

FIG. 3. Trends (shadings) and climatological distributions (contours with an interval of 20 gpm, positive and negative values are depicted by solid and dashed lines respectively, zeroes are depicted by thick solid lines) of southern hemispheric (a) 500 hPa geopotential height zonal deviations with their (b) wave-1 component and (c)

wave-2 component in September during 2000−2017 derived from MERRA-2 dataset. Trends of southern hemispheric (d) tropospheric E-P flux (arrows, units of horizontal and vertical components are 3×10^5 and 3×10^3 kg s^{-2} per year, respectively) and its vertical component (shading) with their (e) wave-1 component and (f) wave-2 component in September during 2000−2017 derived from MERRA-2 dataset. The stippled regions represent the trend significant at/above the 90% confidence level.

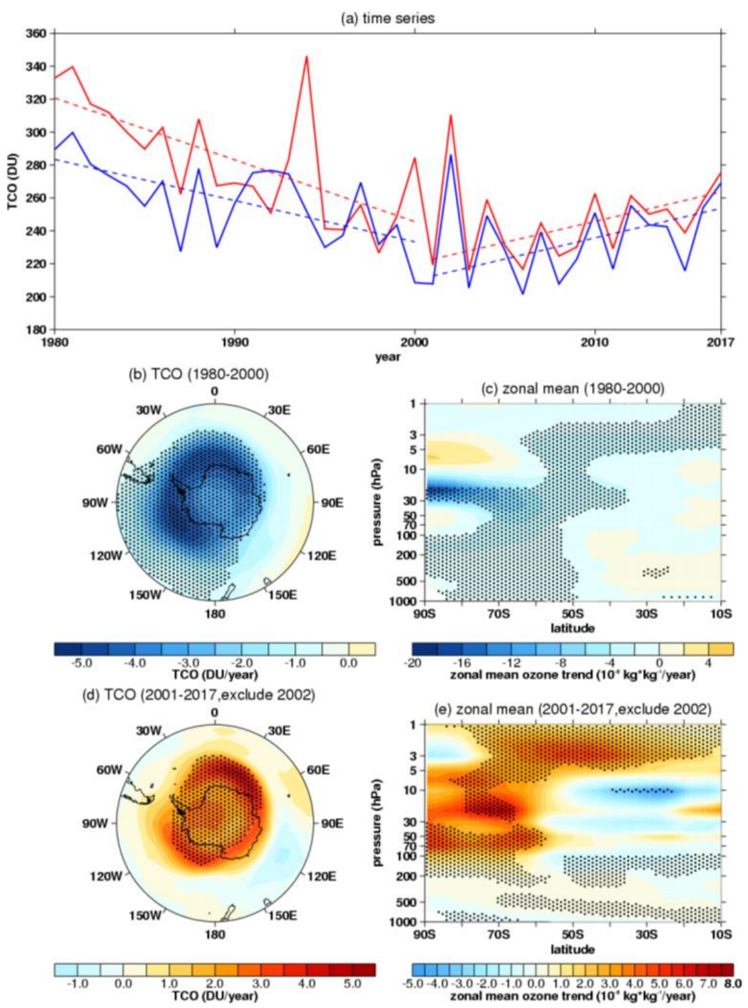

带格式的: 居中

FIG. 4. (a) Time series (solid lines) of aera-weighted total column ozone (TCO) over 60°S to 90°S derived from MERRA-2 (red) and SBUV (blue) datasets. The dashed lines represent linear regression of TCO. (b, d) The TCO trends in September during 1980-2000 (b) and 2001-2017 (d) derived from MERRA-2 dataset. The outermost latitudes in Figs. 4c, d are both 40°S. (c, e) The zonal mean ozone trends on latitude-pressure profile in September during 1980-2000 (c) and 2001-2017 (e) derived from MERRA-2 dataset. The stippled regions in Figs. 4b-e represent trends significant at/above the 90% confidence level. Data in 2002 are removed when trends, regressions and significances are calculated in Fig. 4.

带格式的: 字体: 加粗

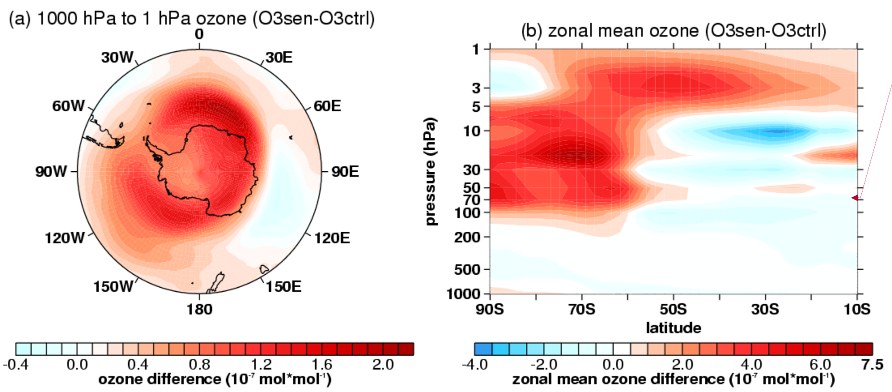

带格式的: 居中

FIG. 5. (a) Difference of horizontal ozone forcing field averaged from 1000 hPa to 1 hPa between O3sen and O3ctrl. The outermost latitude in Fig. 5a is 40°S. (b) Zonal mean difference of ozone forcing fields on latitude-pressure profile in the southern hemisphere between O3sen and O3ctrl.

带格式的: 字体: 加粗

带格式的: 字体: 非加粗

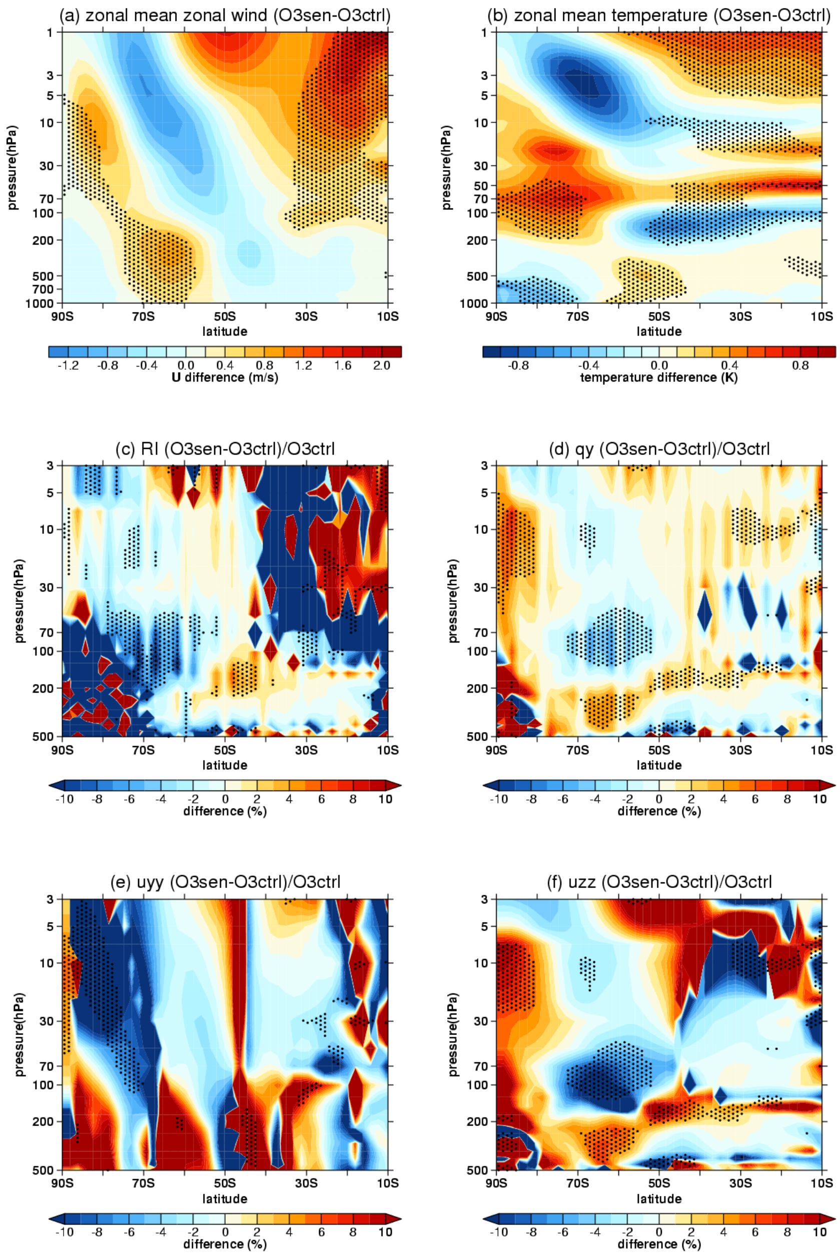

FIG. 6. Difference of (a) zonally averaged zonal wind, (b) zonally averaged

带格式的: 居中

带格式的: 字体: 加粗

temperature, (c) refractive index, (d) $a^2\bar{q}_\varphi$, (e) $-[\frac{(\bar{u}\cos\varphi)_\varphi}{\cos\varphi}]_\varphi$ (uyy term), (f) $-\frac{a^2 f^2}{\rho_0}(\rho_0 \frac{\bar{u}_z}{N^2})_z$ (uzz term) between O3sen and O3ctrl. The stippled regions represent the difference significant at/above 90% confidence level.

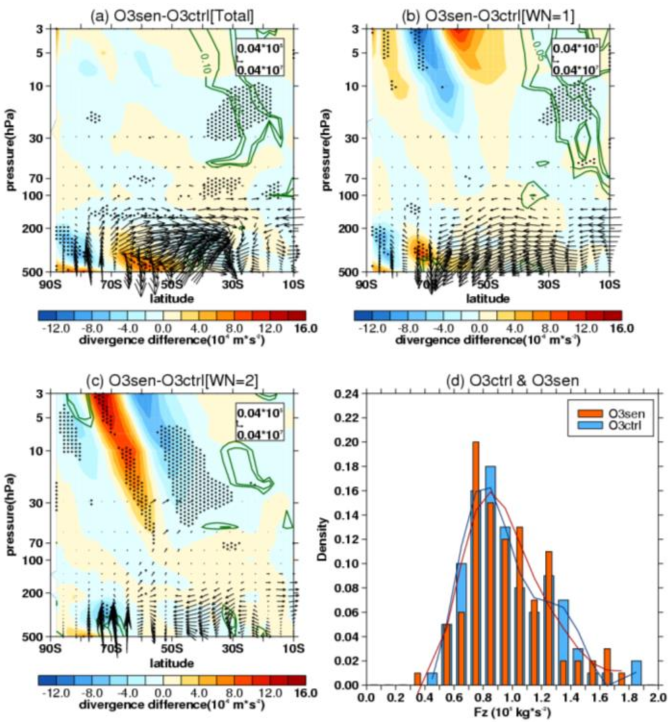

FIG. 7. Differences of (a) stratospheric E-P flux (arrows, units in horizontal and vertical components are 0.04×10^7 and 0.04×10^5 kg s^{-2}, respectively) and its divergence (shadings) with their (b) wave-1 component and (c) wave-2 component between the sensitive experiment (O3sen) and the control experiment (O3ctrl). The stippled regions represent the mean differences of E-P flux divergence significant at/above the 90% confidence level. The green contours from outside to inside (corresponding to p=0.1, 0.05) represent the mean differences of vertical E-P flux significant at the 90% and 95%

域代码已更改
域代码已更改
域代码已更改
带格式的: 居中
带格式的: 字体: 加粗
带格式的: 字体: 加粗

confidence levels, respectively. (d) Frequency distributions (pillars, blue for O3ctrl and orange for O3sen) of vertical E-P flux (Fz, area-weighted from 200 hPa to 10 hPa over 70 °S-50 °S) and it 5-point low-pass filtered fitting curves (solid lines, blue for O3ctrl and red for O3sen) derived from 100 ensemble members.

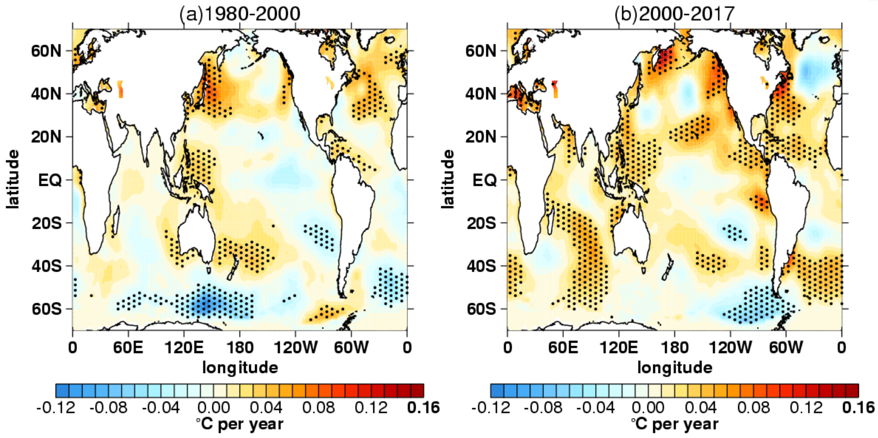

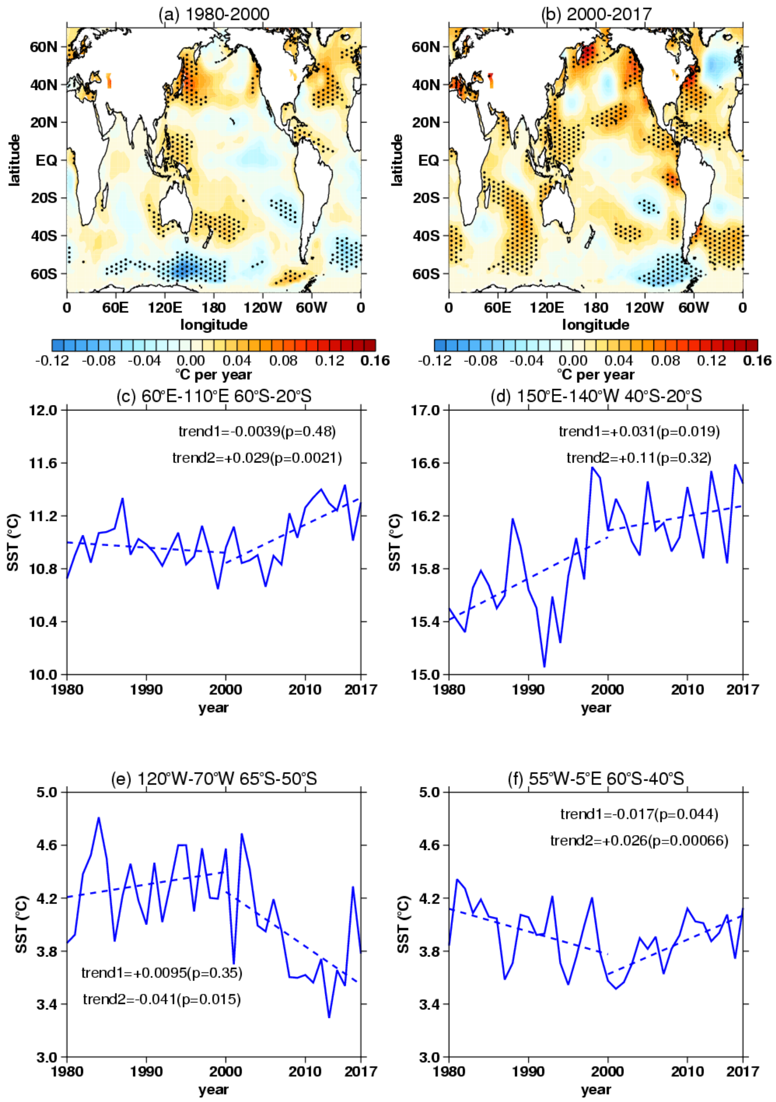

FIG. 48. Trends of SST in September over (a) 1980-2000 and (b) 2000-2017 derived from ERSST v5 dataset. The stippled regions represent the trends significant at/above the 90% confidence level. (c-f) Time series (blue solid lines) of SST during 1980-2017 over different regions (titles). The dashed lines represent linear regressions of SST time series on piecewise periods (1980-2000 and 2000-2017). The “trend1” and “trend2”

labeled in Figs. 8c-f represent the trend coefficients and the corresponding significances (bracketed) over 1980-2000 and 2000-2017, respectively.

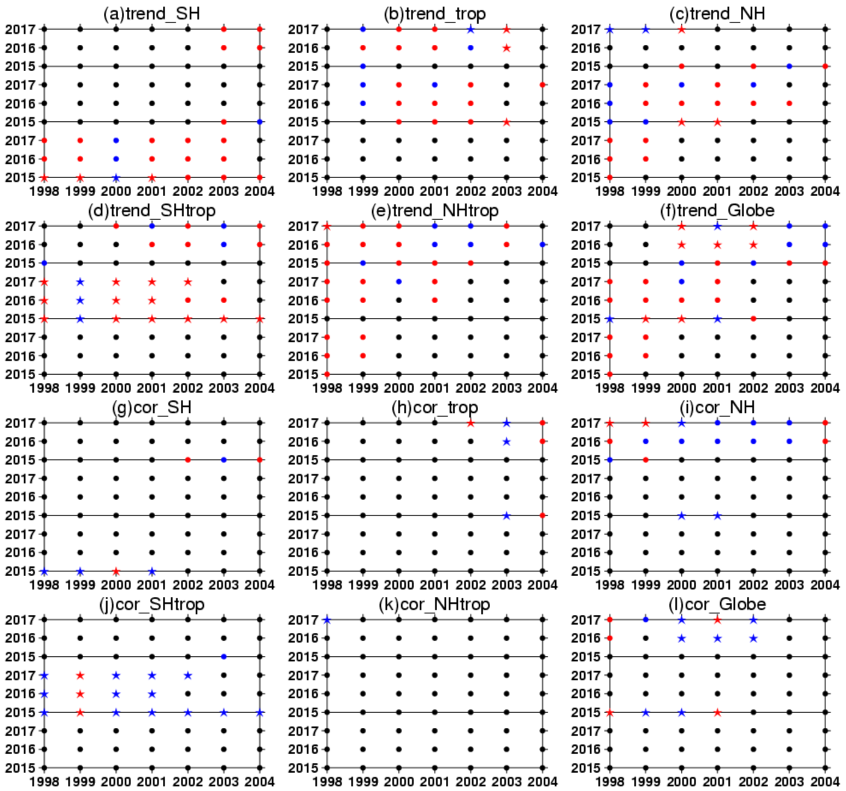

FIG. ~~5~~9. Trend significance of the first three SST principal components (PCs) in (a) the extratropical southern hemisphere (SH, 70°S-20°S), (b) the tropics (TROP, 20°S-20°N), (c) the extratropical northern hemisphere (NH, 20°N-70°N), (d) the extratropical southern hemisphere and the tropics (SHtrop, 70°S-20°N), (e) the extratropical northern hemisphere and the tropics (NHtrop, 20°S-70°N), (f) the globe (70°S-70°N) and the corresponding (g, h, i, j, k, l) correlation significances between them and vertical E-P flux (Fz, area-weighted from 100 hPa to 30 hPa over 70°S-50°S) during different beginning years (x-axes) and ending years (y-axes). The red and blue dots indicate positive and negative trend or correlation coefficient are significant, respectively. The black dots indicate the trends or correlation coefficients are not significant. The stars indicate that the trends and the corresponding correlation coefficients are both significant. Each panel is divided into three regions from bottom to top, corresponding to the first, the second and the third principal components, respectively. The criterion to distinguish whether the trends and correlations are significant or not is the 90% confidence level.

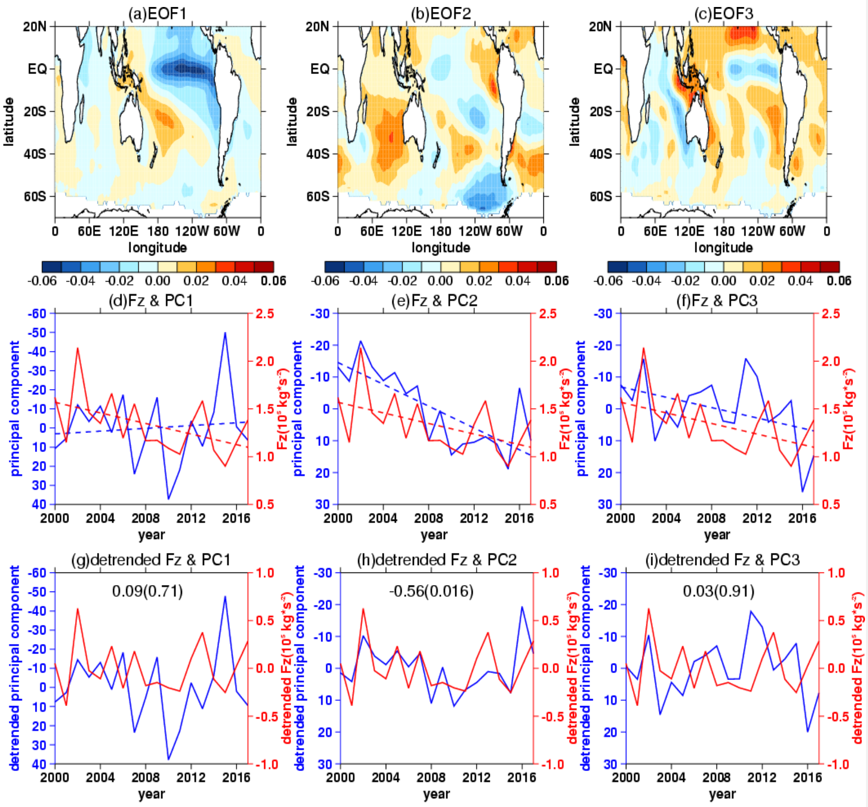

FIG. ~~6~~10. (a, b, c) The first three EOF patterns of SST in SHtrop region. (d, e, f) The original time series of the first three principle components (PCs, blue solid lines correspond to left inverted y-axes) and stratospheric vertical E-P flux (Fz, area-weighted from 100 hPa to 30 hPa over 70°S-50°S, red solid lines correspond to right y-axes) in September during 2000-2017. The blue and red dashed lines in (d, e, f) represent the linear regressions of PC time series and Fz time series, respectively. The meaning of (g, h, i) are the same as (d, e, f) correspondingly, except the detrended time series. The unbracketed and bracketed numbers in (g, h, i) represent the correlation coefficients between detrended PC time series and Fz time series and the corresponding p values calculated by two-tailed t test, respectively.

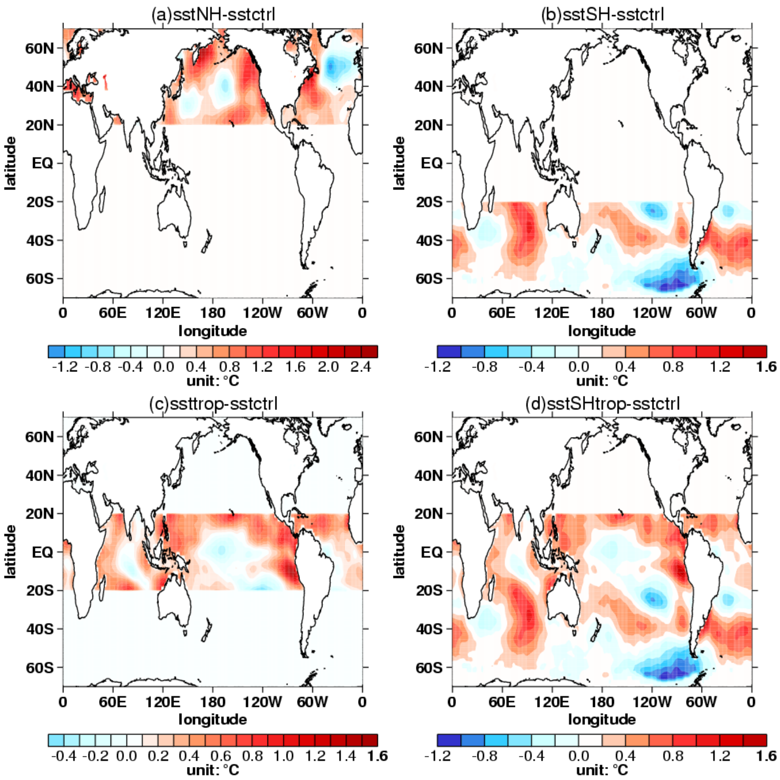

FIG. ~~7~~11. Differences in SST forcing field between sensitive experiments ((a) sstNH; (b) sstSH; (c) ssttrop; (d) sstSHtrop) and the control experiment (sstctrl).

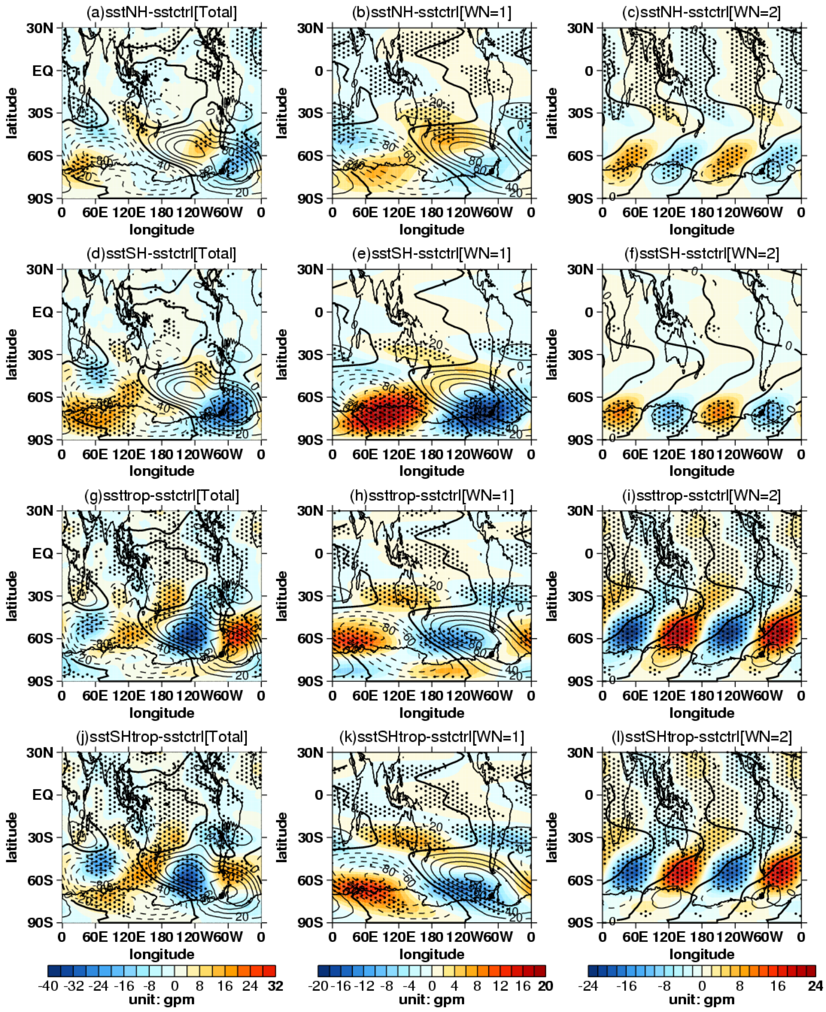

FIG. ~~8~~12. Differences (shadings) of (a, d, g, j) 500 hPa geopotential height zonal deviations with their (b, e, h, k) wave-1 component and (c, f, i, l) wave-2 component between sensitive experiments ((a, b, c) sstNH; (d, e, f) sstSH; (g, h, i) ssttrop; (j, k, l) sstSHtrop) and the control experiment (sstctrl). The mean distributions (contours with an interval of 20 gpm, positive and negative values are depicted by solid and dashed lines respectively, zeroes are depicted by thick solid lines) of them are derived from the control experiment. The stippled regions represent the mean difference significant at/above the 90% confidence level.

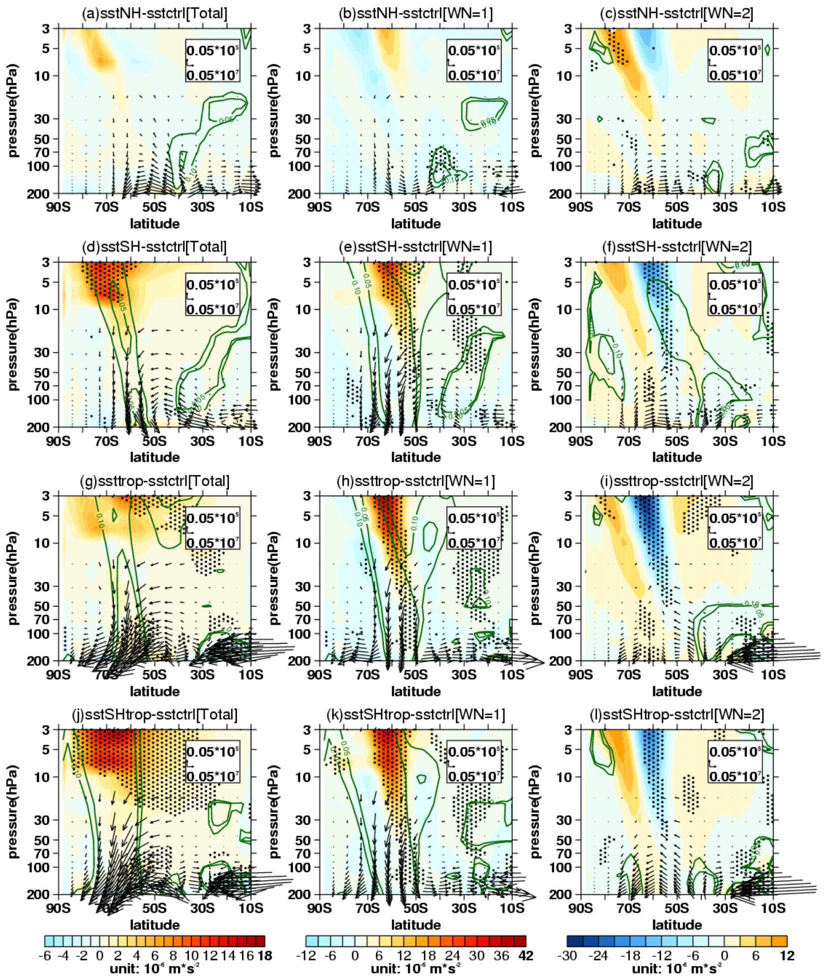

FIG. ~~9~~13. Differences of (a, d, g, j) stratospheric E-P flux (arrows, units in horizontal and vertical components are 0.05×10^{7} and 0.05×10^{5} $kg\cdot s^{-2}$, respectively) and its divergence (shadings) with their (b, e, h, k) wave-1 component and (c, f, i, l) wave-2 component between sensitive experiments ((a, b, c) sstNH; (d, e, f) sstSH; (g, h, i) ssttrop; (j, k, l) sstSHtrop) and the control experiment (sstctrl). The stippled regions represent the mean differences of E-P flux divergence significant at/above the 90% confidence level. The green contours from outside to inside (corresponding to p=0.1, 0.05) represent the mean differences of vertical E-P flux significant at the 90% and 95% confidence levels, respectively.

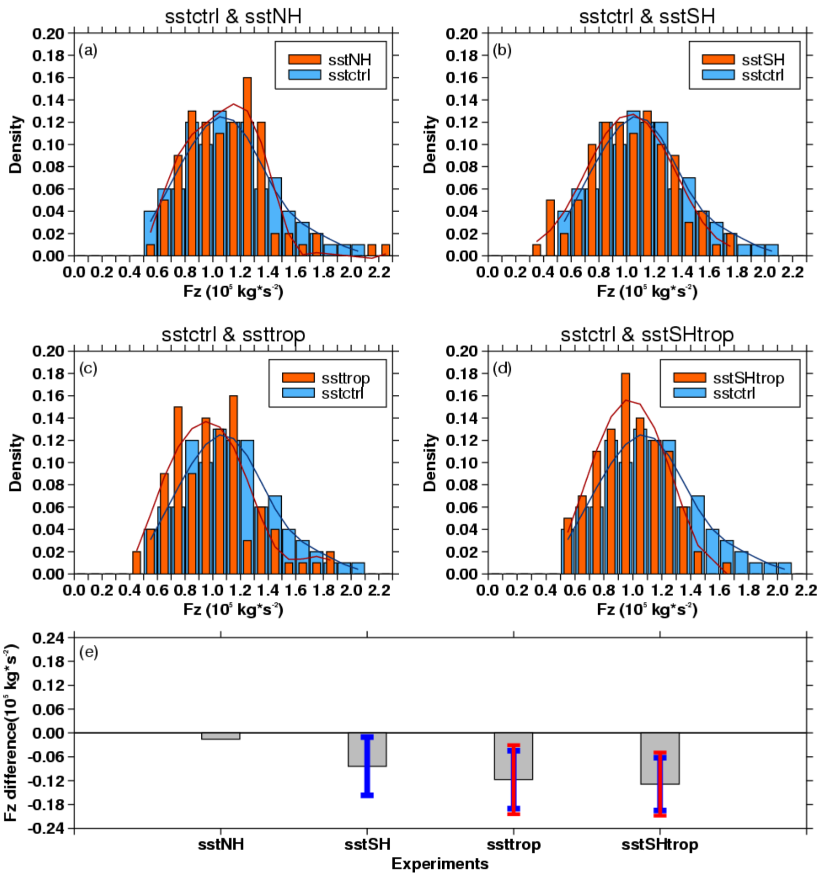

FIG. ~~10~~14. (a, b, c, d) Frequency distributions (pillars, blue for control experiment and orange for sensitive experiments) of vertical E-P flux (Fz, area-weighted from 200 hPa to 10 hPa over 70°S-50°S) and its 5-point low-pass filtered fitting curves (solid lines, blue for control experiment and red for sensitive experiments) derived from 100 ensemble members of the control experiment (sstctrl) and sensitive experiments ((a) sstNH; (b) sstSH; (c) ssttrop; (d) sstSHtrop), respectively. (e) Mean differences (grey pillars) and corresponding uncertainties (error bars) of Fz between sensitive experiments and the control experiment. The blue and red error bars reflect the 90% and 95% confidence levels calculated by two-tailed t test, respectively. The error bar is omitted when the significance of mean difference is lower than the corresponding confidence level.

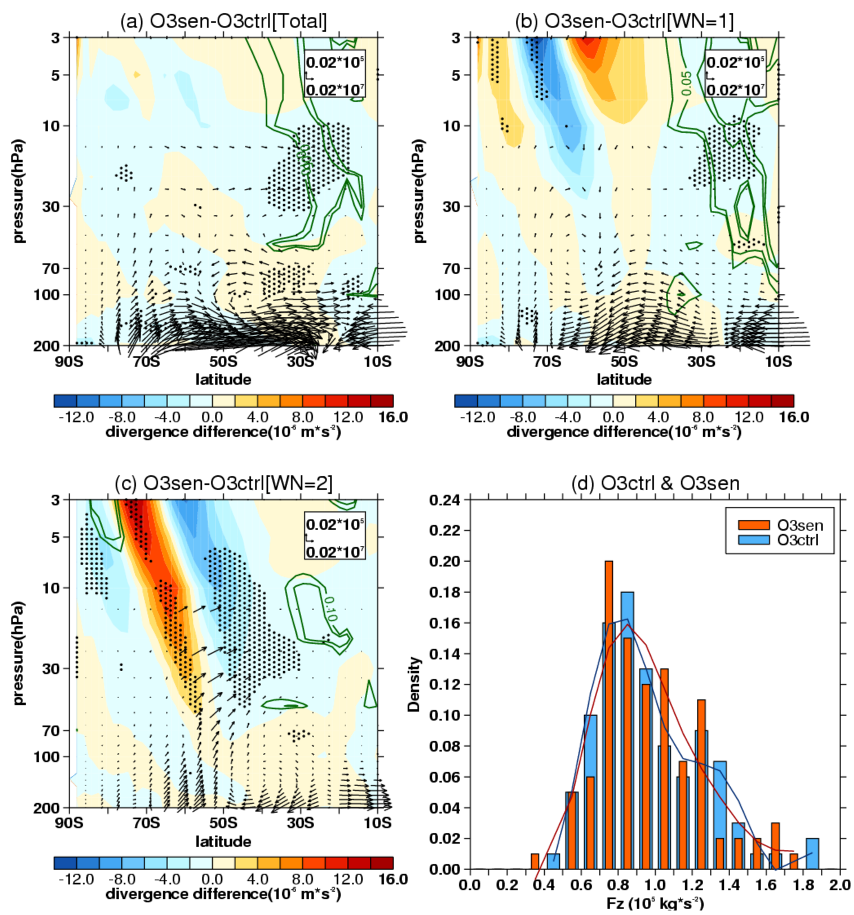

~~FIG. 11.~~ ~~Differences of (a) stratospheric E-P flux (arrows, units in horizontal and~~

~~vertical components are 0.02×10^{7} and 0.05×10^{5} kg·s^{-2}, respectively) and its divergence (shadings) with their (b) wave 1 component and (c) wave 2 component between the sensitive experiment (O3sen) and the control experiment (O3ctrl). The stippled regions represent the mean differences of E-P flux divergence significant at/above the 90% confidence level. The green contours from outside to inside (corresponding to p=0.1, 0.05) represent the mean differences of vertical E-P flux significant at the 90% and 95% confidence levels, respectively. (d) Frequency distributions (pillars, blue for O3ctrl and orange for O3sen) of vertical E-P flux (Fz, area-weighted from 200 hPa to 10 hPa over 70°S-50°S) and it 5-point low-pass filtered fitting curves (solid lines, blue for O3ctrl and red for O3sen) derived from 100 ensemble members.~~

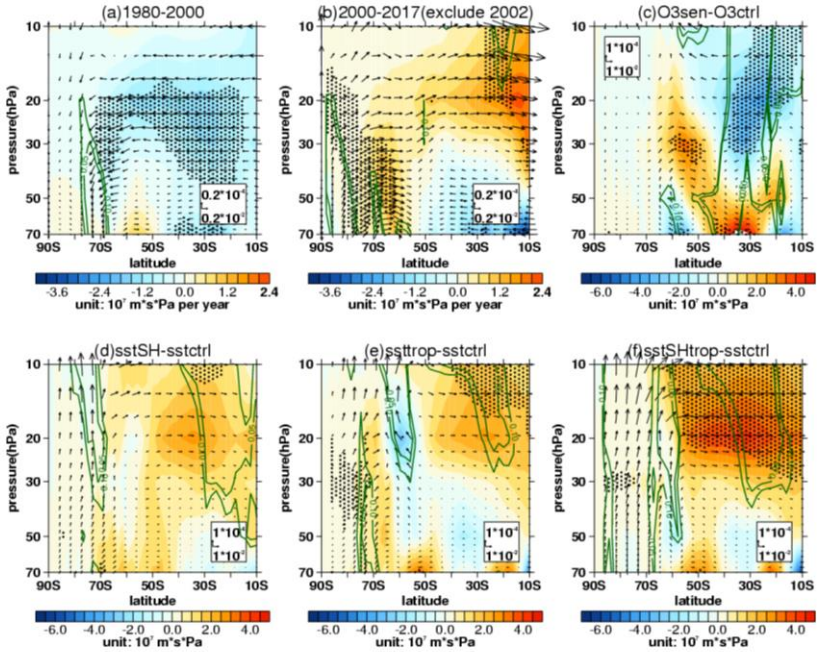

FIG. ~~12~~15. (a) Trends of southern hemispheric Brewer-Dobson circulation (arrows, units in horizontal and vertical components are 0.2×10^{-2} and 0.2×10^{-4} m·s^{-1} per year, respectively) and its stream function (shadings) in September during (a) 1980-2000 and (b) 2000-2017 derived from MERRA-2 dataset. Data in 2002 are removed when trends are calculated in Figure (b). (c) Differences of Brewer-Dobson circulation (arrows, units in horizontal and vertical components are 10^{-2} and 10^{-4} $m \cdot s^{-1}$, respectively) and its stream function (shadings) between the O3ctrl and O3sen. (d, e, f) Differences of Brewer-Dobson circulation and its stream function between the control experiment (sstctrl) and ~~various~~ sensitive experiments ((d) sstSH; (e) ssttrop; (f) sstSHtrop) with SST changes. The stippled regions represent the trends or differences of the stream function significant at/above the 90% confidence level. The green contours from outside to inside (corresponding to p=0.1, 0.05) represent the trends or differences of the vertical components significant at the 90% and 95% confidence levels, respectively.